Off-Resonance Correction of MR Images

Hermann Schomberg, *Member, IEEE*

***Abstract*— In magnetic resonance imaging (MRI), the spatial inhomogeneity of the static magnetic field can cause degraded images if the reconstruction is based on inverse Fourier transformation. This paper presents and discusses a range of fast reconstruction algorithms that attempt to avoid such degradation by taking the field inhomogeneity into account. Some of these algorithms are new, others are modified versions of known algorithms. Speed and accuracy of all these algorithms are demonstrated using spiral MRI.**

***Index Terms*—Conjugate phase reconstruction, magnetic resonance imaging, off-resonance correction, simulated phase evolution and rewinding.**

I. Introduction

MOST MRI methods generate their images in two steps. First, the object to be imaged is subjected to an MRI experiment of one kind or another and then the image is reconstructed from the outcome of this experiment. The reconstruction algorithm is designed to invert a mathematical model of the experiment. Usually, the Fourier transform is taken as the model and the reconstruction is done by a discrete version of the inverse Fourier transform [1]–[5].

In practice, the assumed Fourier transform relationship between image and data is marred by a number of imperfections, resulting in various kinds of image artifacts if the reconstruction is nevertheless based on inverse Fourier transformation. One of the major imperfections is the spatial inhomogeneity of the static magnetic field, which typically causes distorted or blurred images. This paper presents and discusses a range of fast reconstruction algorithms that attempt to avoid such artifacts by inverting, approximately, an extended model of the MRI experiment that takes the spatial inhomogeneity of the static magnetic field into account. Some of these algorithms are new, others are modified versions of algorithms devised by to Noll *et al.* [6], [7], Man *et al.* [8], and Kadah and Hu [9]. Speed and accuracy of all these algorithms are demonstrated using spiral MRI.

The paper is organized as follows: Section II presents the extended model of the MRI experiment. Section III discusses inversion strategies. Sections IV and V present the reconstruction algorithms. Section VI focuses on spiral MRI. Section VII summarizes the test results. Section VIII concludes the paper with a few remarks.

Notations: The symbols $\mathbb{R}$ and $\mathbb{C}$ denote the sets of real and complex numbers, respectively. The n-fold Cartesian product of $\mathbb{R}$ and $\mathbb{C}$ is denoted by $\mathbb{R}^n$ and $\mathbb{C}^n$, respectively. An interval of the form $\{x \in \mathbb{R} | a \le x \le b\}$ is abbreviated by $[a, b]$. The notation $f\colon X \to Y$ indicates a mapping (function) f with domain X and range Y. The concatenation of two mappings $f\colon X \to Y$ and $g\colon Y \to Z$ is the mapping $g \circ f\colon X \to Z$ defined by $(g \circ f)(x) = g(f(x))$. The partial derivative of a differentiable function $f\colon \mathbb{R}^n \to \mathbb{R}$ with respect to the jth variable is written as $\partial_j f$. The Hilbert space of square-integrable functions $h\colon \mathbb{R}^n \to \mathbb{C}$ is denoted by $L_2(\mathbb{R}^n)$.

Manuscript received July 28, 1997; revised October 30, 1998. The Associate Editor responsible for coordinating the review of this paper and recommending its publication was X. Hu.

The author is with Philips Research, 22335 Hamburg, Germany (e-mail: H.Schomberg@pfh.research.philips.com).

Publisher Item Identifier S 0278-0062(99)06611-2.

II. An Extended Model of the MRI Experiment

Underlying the considerations in Sections II–V is a typical two-dimensional (2-D) MRI method implemented on a typical MRI system [5]. We attach a right-handed, Cartesian (x_1, x_2, x_3)-coordinate system to the main magnet such that the origin of this system lies in the isocenter of the main magnet and the x_3-axis is parallel to the main magnetic field. Any direction perpendicular to the x_3-axis is referred to as transverse. The generalization to three-dimensional (3-D) MRI methods is conceptually straightforward.

Prior to the MRI experiment, the object to be imaged (in medical applications, the patient) is placed inside the bore of the magnet. For simplicity we assume that the slice to be imaged corresponds to the transverse plane $x_3 = 0$. The spatial variable in this plane is written as $\mathbf{x} = (x_1, x_2)$. The time variable is denoted by t. The object is supposed to stay at rest during the experiment.

The experiment itself consists of a sequence of $M \ge 1$ subexperiments. All subexperiments have the same duration (repetition time), the same structure, and follow immediately upon each other. Each subexperiment, in turn, consists of an excitation phase, a preparation phase, an acquisition phase, and a recovery phase. When imaging a transverse slice, only a transverse gradient field is used during the acquisition phase. See, e.g., [5] for more information about MRI experiments and the numerous variations possible.

The subexperiments are designed to be time-shift invariant. So we can pretend that each subexperiment occurs in the same time interval. We denote the beginning and the end of the acquisition phase by τ_- and τ_+, respectively, so that

$$T = \tau_+ - \tau_- \tag{1}$$

is the duration of the acquisition phase (acquisition time). The (demodulated) MR signal acquired during the acquisition phase of the mth subexperiment is represented by a function $s_m\colon [\tau_-, \tau_+] \to \mathbb{C}$. Each MR signal is sampled at the N time points

$$t_n = \tau_- + nT/N, \qquad 0 \le n < N. \tag{2}$$

The outcome of the MRI experiment consists of the MN complex numbers $s_m(t_n)$, $0 \le m < M$, $0 \le n < N$.

The transverse magnetization in the plane $x_3 = 0$ at the beginning of the preparation phase is independent of m and t and conveniently described by a function $M_\perp$: $\mathbb{R}^2 \to \mathbb{C}$, whose real and imaginary parts correspond to the x_1- and x_2-components of the transverse magnetization, respectively. The support of $M_\perp$ is contained in some region R in $\mathbf{x}$-space, such as the square

$$R_\square(r_{\max}) = \{\mathbf{x} \in \mathbb{R}^2 \,|\, |x_1|, |x_2| \le r_{\max}\} \tag{3}$$

or the disk

$$R_\circ(r_{\max}) = \{\mathbf{x} \in \mathbb{R}^2 \,|\, (x_1^2 + x_2^2)^{1/2} \le r_{\max}\} \tag{4}$$

for some known $r_{\max} > 0$. The magnitude of $M_\perp$ is closely related to the proton density of the object, but also depends on the MRI system and the experiment. The phase of $M_\perp$ depends on various factors, but is often independent of the object.

By tracking the time evolution of the transverse magnetization and modeling the signal reception process one can show, similarly to the standard $\mathbf{k}$-space description of MRI [1]–[5], that the functions s_m and $M_\perp$ are related according to

$$s_m(t) = \int_{\mathbb{R}^2} W(\mathbf{x}) M_\perp(\mathbf{x}) e^{-i\omega(\mathbf{x})(t-\tau_-)} e^{-i\mathbf{x}\cdot\mathbf{p}_m(t)}\, d\mathbf{x} + \epsilon_m(t), \quad 0 \le m < M,\ t \in [\tau_-, \tau_+] \tag{5}$$

where W: $\mathbb{R}^2 \to \mathbb{C}$ is a weighting function, ω: $\mathbb{R}^2 \to \mathbb{R}$ a "frequency map," $\mathbf{p}_m$: $[\tau_-, \tau_+] \to \mathbb{R}^2$ a path or trajectory in so-called $\mathbf{k}$-space, and ϵ_m: $[\tau_-, \tau_+] \to \mathbb{C}$ an error term. These functions are further explained below.

The frequency map ω (also known as off-resonance map or field map) is related to the strength of the static magnetic field according to

$$\omega(\mathbf{x}) = \gamma B(\mathbf{x}) - \omega_{\mathrm{RF}} \tag{6}$$

where γ is the gyromagnetic ratio of protons [$\gamma/(2\pi) = 42.6$ MHz/T], $B(\mathbf{x})$ the strength of the static magnetic field at $\mathbf{x}$, and ω_{RF} the demodulation frequency of the receiver. The spatial variation of B and, hence, ω is due to the slight inhomogeneity of the applied static magnetic field and to the spatially varying magnetic susceptibility of the object [10], [11]. In medical MRI, $|\omega(\mathbf{x})/\omega_{\mathrm{RF}}|$ is typically below some 10 parts per minute (ppm) in R. Moreover, ω varies slowly and smoothly with position, except perhaps across the boundaries between biological tissue and air [10]–[12]. The factor $e^{-i\omega(\mathbf{x})(t-\tau_-)}$ of the integrand in (5) describes the off-resonance effect resulting from the spatial inhomogeneity of the static magnetic field during the acquisition phase. Changing ω outside the support of $M_\perp$ does not affect the value of the integral. We exploit this freedom to let ω quickly go to zero outside the support of $M_\perp$, making sure that ω has a bounded support. A condition of this kind is needed for some mathematical arguments at a later stage. For later purposes we also define

$$\omega_- = \min_{\mathbf{x} \in \operatorname{supp} M_\perp} \omega(\mathbf{x}), \qquad \omega_+ = \max_{\mathbf{x} \in \operatorname{supp} M_\perp} \omega(\mathbf{x}), \tag{7}$$

$$\Omega = \omega_+ - \omega_-. \tag{8}$$

The weighting function W in (5) takes various system-, method-, and object-dependent factors into account. If the MRI method under consideration does not employ a π pulse during the preparation phase, W may be written as

$$W(\mathbf{x}) = c\, C_{\mathrm{rc}}(\mathbf{x}) e^{-i\omega(\mathbf{x})T_{\mathrm{p}}} \tag{9}$$

where c is a system- and method-dependent complex constant, T_{p} the duration of the preparation phase (preparation time), and C_{rc} a complex-valued function that is closely related to the sensitivity pattern of the receive coil [13]. The factor $e^{-i\omega(\mathbf{x})T_{\mathrm{p}}}$ in (9) accounts for the off-resonance effect during the preparation phase. If the MRI method does employ a π pulse at time $\tau_- - T_\pi$ with $0 < T_\pi < T_{\mathrm{p}}$, then the weighting function changes to

$$W(\mathbf{x}) = \pm c\, C_{\mathrm{rc}}(\mathbf{x}) e^{i\omega(\mathbf{x})(T_{\mathrm{p}} - 2T_\pi)} \tag{10}$$

where the sign depends on the axis of the π pulse. We regard the function

$$f = W M_\perp \tag{11}$$

as the image of the object that is to be reconstructed from the outcome of the experiment. The phase of f is usually smooth and the support of f equals the support of $M_\perp$. Most morphological information about the object is already conveyed by $|f|$.

The factor $e^{-i\mathbf{x}\cdot\mathbf{p}_m(t)}$ of the integrand in (5) captures the effect of the transverse gradient field during the acquisition phase of the mth subexperiment. The trajectory $\mathbf{p}_m$ is related to the waveform $\mathbf{G}_m$: $[\tau_-, \tau_+] \to \mathbb{R}^2$ of this gradient field by an equation of the form

$$\mathbf{p}_m(t) = \mathbf{p}_m(\tau_-) + \gamma \int_{\tau_-}^{t} \mathbf{G}_m(t')\, dt', \qquad t \in [\tau_-, \tau_+] \tag{12}$$

where the initial value $\mathbf{p}_m(\tau_-)$ depends on the details of the preparation phase. These initial values and the gradient waveforms are chosen such that the trajectories fill a centered region S in $\mathbf{k}$ space, such as the square

$$S_\square(\hat{r}_{\max}) = \{\mathbf{k} \in \mathbb{R}^2 \,|\, |k_1|, |k_2| \le \hat{r}_{\max}\} \tag{13}$$

or the disk

$$S_\circ(\hat{r}_{\max}) = \{\mathbf{k} \in \mathbb{R}^2 \,|\, (k_1^2 + k_2^2)^{1/2} \le \hat{r}_{\max}\} \tag{14}$$

for some known $\hat{r}_{\max} > 0$. [We let $\mathbf{k} = (k_1, k_2)$ in analogy to $\mathbf{x} = (x_1, x_2)$.] The grid points or sampling points $\mathbf{p}_m(t_n)$ form a certain pattern in S, the "sampling pattern."

Finally, the function ϵ_m in (5) closes the gap between the function s_m on the left and its postulated integral representation on the right. Such a gap is caused by the numerous idealizations underlying the derivation of (5). For example, the derivation ignores relaxation effects, the chemical shift between fat and water, the effects of eddy currents, and the

x_3-dependency of W, $M_\perp$, and ω. In addition, the MR signals are cluttered by noise. (Yet ϵ_m is a function, not a random variable.) The error term is unknown, but expected to be small.

Omitting the term $e^{-i\omega(\mathbf{x})(t-\tau_-)}$ under the integral sign in (5) yields the standard $\mathbf{k}$-space description of the MRI experiment, but also increases the error term.

MRI methods may be classified by their trajectories and sampling patterns. In spin warp MRI [14] and its relatives, the trajectories are chosen as straight equidistantly spaced lines parallel to the k_1-axis (for example) and the sampling points form a Cartesian grid in $S_\square(\hat{r}_{\max})$. Similar grids arise with blipped echo planar imaging (EPI) [15]–[17]. We refer to all such methods as Cartesian MRI. In spiral MRI [18]–[20], the trajectories are chosen as interleaved archimedian spirals starting at the origin of $\mathbf{k}$-space, resulting in a spiral sampling pattern in $S_\circ(\hat{r}_{\max})$. In radial MRI [21], [22], the trajectories are chosen as straight radial lines, resulting in a radial sampling pattern in $S_\circ(\hat{r}_{\max})$.

To facilitate the reasoning about inversion strategies and reconstruction algorithms, it is advisable to extend the semi-continuous equation (5) to a fully continuous equation between functions in $L_2(\mathbb{R}^2)$. As the first and major step toward this end, we try to establish an operator $\mathcal{M}$ in $L_2(\mathbb{R}^2)$ such that (5) may be rewritten as

$$s_m(t) = (\mathcal{M}f)(\mathbf{p}_m(t)) + \epsilon_m(t), \qquad 0 \le m < M,\ t \in [\tau_-, \tau_+]. \quad (15)$$

The standard $\mathbf{k}$-space description of MRI suggests to decompose $\mathcal{M}$ in the form

$$\mathcal{M} = \mathcal{F} + \mathcal{P} \quad (16)$$

where $\mathcal{F}$ is the 2-D Fourier transform as defined by

$$(\mathcal{F}f)(\mathbf{k}) = \int_{\mathbb{R}^2} f(\mathbf{x}) e^{-i\mathbf{x}\cdot\mathbf{k}}\, d\mathbf{x} \quad (17)$$

and $\mathcal{P}$ is a perturbing operator that takes the off-resonance effect into account. An equivalent decomposition of $\mathcal{M}$ is $\mathcal{M} = \mathcal{F}(\mathcal{I} + \mathcal{F}^{-1}\mathcal{P})$ where $\mathcal{I}$ is the identity operator in $L_2(\mathbb{R}^2)$.

To be able to define $\mathcal{P}$, we request that the MRI method under consideration admit a "time map" τ: $\mathbb{R}^2 \to \mathbb{R}$ such that

$$\tau(\mathbf{p}_m(t_n)) = t_n - \tau_-, \qquad 0 \le m < M,\ 0 \le n < N. \quad (18)$$

Such a time map exists if the trajectories do not intersect or, if they do, all trajectories intersecting at a point visit that point at the same time (time shift of the subexperiments understood). Under these conditions, we can define τ at the grid points $\mathbf{p}_m(t_n)$ by (18) and then extend τ onto all of S. The extension is somewhat arbitrary, but usually there is a natural choice. For mathematical convenience at a later stage, we let τ quickly go to zero outside S, making sure that τ has a bounded support. Without loss of generality we may assume that

$$\min_{\mathbf{k}\in S} \tau(\mathbf{k}) = 0, \qquad \max_{\mathbf{k}\in S} \tau(\mathbf{k}) = T. \quad (19)$$

All major MRI methods do admit a time map. Even more, many MRI methods, including the standard versions of Cartesian, spiral, and radial MRI, have natural time maps that may be expressed in closed form. For example, the natural time map of spin-warp MRI is

$$\tau(\mathbf{k}) = \begin{cases} (1 + k_1/\hat{r}_{\max})T/2, & \text{if } \mathbf{k} \in S_\square(\hat{r}_{\max}) \\ 0, & \text{else.} \end{cases} \quad (20)$$

In addition, the natural time maps of the standard versions of Cartesian, spiral, and radial MRI are continuous in S. Other natural time maps, in particular those of some segmented versions of blipped EPI [16], [17] or of ring-segmented spiral MRI [23], are discontinuous in S.

Assuming from now on the existence of a time map, we define $\mathcal{P}$ by the formula

$$(\mathcal{P}f)(\mathbf{k}) = \int_{\mathbb{R}^2} f(\mathbf{x})\Big(e^{-i\omega(\mathbf{x})\tau(\mathbf{k})} - 1\Big)e^{-i\mathbf{x}\cdot\mathbf{k}}\, d\mathbf{x}. \quad (21)$$

The bounded supports of ω and τ make $\mathcal{P}$ a compact operator of the Hilbert–Schmidt type [24, ch. VI]. The sum $\mathcal{M} = \mathcal{F}+\mathcal{P}$ is then a linear continuous operator in $L_2(\mathbb{R}^2)$ and given by

$$(\mathcal{M}f)(\mathbf{k}) = \int_{\mathbb{R}^2} f(\mathbf{x}) e^{-i\omega(\mathbf{x})\tau(\mathbf{k})} e^{-i\mathbf{x}\cdot\mathbf{k}}\, d\mathbf{x}. \quad (22)$$

It follows from (5), (18), and (22) that $\mathcal{M}$ satisfies (15), as desired.

As the second and minor step, we extend the MR data onto all of $\mathbf{k}$-space by picking a function $g \in L_2(\mathbb{R}^2)$ that satisfies

$$g(\mathbf{p}_m(t_n)) = s_m(t_n), \qquad 0 \le m < M,\ 0 \le n < N. \quad (23)$$

In addition, g is to be well-behaved in between the sampling points and to vanish outside S.

It now follows from (15) and (23) that

$$\mathcal{M}f = g + \epsilon \quad (24)$$

where $\epsilon \in L_2(\mathbb{R}^2)$ closes the gap between $\mathcal{M}f$ and g and satisfies

$$\epsilon(\mathbf{p}_m(t_n)) = -\epsilon_m(t_n), \qquad 0 \le m < M,\ 0 \le n < N. \quad (25)$$

Equation (24) is the wanted fully continuous companion of (5). The operator $\mathcal{M}$ may be regarded as an extended model of the MRI experiment and will be referred to as the MR transform. Since $\mathcal{F}^{-1}\mathcal{P}$ is also compact, the Fredholm alternative holds for $\mathcal{F}^{-1}\mathcal{M} = \mathcal{I} + \mathcal{F}^{-1}\mathcal{P}$ as well as for $\mathcal{M}$ [24, ch. VI]. Unlike the standard model, $\mathcal{F}$, the extended model depends on the MRI system and the MRI experiment (via ω and τ) and even on the object (via ω). We write $\mathcal{M}[\omega, \tau]$ if we want to emphasize this dependency. The values of τ outside S have no effect on the values of $\mathcal{M}f$ in S so that our decision to let τ go to zero outside S does not affect the validity of the model. Setting g to zero outside S is in line with our lack of measurements outside S and the observation that $\mathcal{M}f$, which equals $\mathcal{F}f$ outside the support of τ, tends to zero as $|\mathbf{k}| \to \infty$.

It is not strictly necessary that ω and τ have a bounded support. For example, if ω_0 and τ_0 are arbitrary real constants, then the function $e^{i\omega_0(\tau-\tau_0)}\mathcal{M}[\omega, \tau](e^{i\omega\tau_0} f)$ belongs to $L_2(\mathbb{R}^2)$

$$\mathcal{M}[\omega - \omega_0, \tau - \tau_0]f = e^{i\omega_0(\tau-\tau_0)}\mathcal{M}[\omega, \tau](e^{i\omega\tau_0} f). \quad (26)$$

In the standard approach to MRI, $\mathcal{F}$ is taken as model and f reconstructed by computing a discrete approximation to $\mathcal{F}^{-1}g$ in R, using the available samples of g in S. It follows from (16) and (24) that

$$\mathcal{F}^{-1}g = f + \mathcal{F}^{-1}\mathcal{P}f - \mathcal{F}^{-1}\epsilon \tag{27}$$

which shows that the accuracy of the reconstruction is affected by the size of ϵ as well as by the size of $\mathcal{P}f$. The term $\mathcal{F}^{-1}\mathcal{P}f$ in (27) represents a continuous (as opposed to discrete) version of the off-resonance artifact. The accuracy of the result is also affected by the size of S, the density of the sampling pattern in S, and the choice of the reconstruction algorithm. Henceforth, an MR image reconstructed by inverse Fourier transformation will be called a standard image.

Whether the off-resonance artifact present in a standard image is acceptable depends on its size and nature. As is well known, the off-resonance artifact manifests itself mainly as distortion in Cartesian MRI [25] and mainly as blurring in spiral and radial MRI [7]. While a moderate distortion may be tolerable, blurring is generally not.

The size of the off-resonance artifact grows with both Ω and T. More precisely, the value of the expression $\Omega T/(2\pi)$ equals the number of extra turns made during the acquisition phase by the transverse magnetization at a point $\mathbf{x}_+$ with $\omega(\mathbf{x}_+) = \omega_+$, relative to the transverse magnetization at a point $\mathbf{x}_-$ with $\omega(\mathbf{x}_-) = \omega_-$. This number of extra turns can be significant. For example, when $\omega_{\mathrm{RF}}/\gamma = 1$ T, $\Omega/\omega_{\mathrm{RF}} = 5$ ppm, and $T = 20$ ms, then $\Omega T/(2\pi) = 4.26$.

It is always possible to reduce the size of ΩT by reducing T. However, according to (12), if the shape of the trajectories and the size of S are not to be altered, the reduction of T must be compensated for by an increase of the gradient strength, which is possible only to a limited extent. When this possibility is exhausted, one must shorten the lengths of the trajectories in S, which means that more trajectories are needed to cover S with the required density. In other words, one is left with increasing the number of subexperiments. This, however, increases the total duration of the MRI experiment, which is generally undesirable.

Another approach for reducing the off-resonance artifacts consists of computing a discrete approximation to

$$\mathcal{M}^{-1}g = f - \mathcal{M}^{-1}\epsilon. \tag{28}$$

Since $\mathcal{F}^{-1}\mathcal{P}$ is compact, the spectrum of $\mathcal{F}^{-1}\mathcal{P}$ contains only isolated eigenvalues with at most one accumulation point at $\lambda = 0$ [24, Th. VI.15]. Therefore, $\mathcal{M}^{-1}$ exists unless -1 happens to be an eigenvalue of $\mathcal{F}^{-1}\mathcal{P}$. Also, as a consequence of the Fredholm alternative and the inverse mapping theorem, $\mathcal{M}^{-1}$ is continuous if it exists [24]. Thus, as long as no eigenvalue of $\mathcal{F}^{-1}\mathcal{P}$ is close to -1, the term $\mathcal{M}^{-1}\epsilon$ in (28) will not blow up and $\mathcal{M}^{-1}g$ will be close to f. Ideally, an image reconstructed in this way would have no off-resonance artifact.

For this approach the frequency and time maps must be known. While the time map is known at least at the grid points $\mathbf{p}_m(t_n)$, an accurate estimate of the frequency map is difficult to obtain. Fortunately, the ω-dependency of W and thus of f [cf. (9)–(11)] makes it possible to extract a first guess of ω from two standard images obtained with slightly different preparation times [25]. The resulting frequency map will be degraded by the off-resonance artifacts present in the two standard images, but as long as these artifacts are small, a frequency map obtained in this way may yet be usable. If one is willing to spend the effort, one can reconstruct the two images again, this time based on (28) and the current guess of the frequency map, and extract an iterated frequency map from the two newly reconstructed images. The process may be continued. Nevertheless, in practice only some more or less accurate estimate of the frequency map will be available. As a result, an image reconstructed via (28) may still show artifacts caused by the imperfections of the frequency map.

Once ω has been estimated and f reconstructed, one can also recover $cC_{\mathrm{rc}}\mathcal{M}_\perp$ using (9) and (11) or (10) and (11), as appropriate. Under a wide range of circumstances, the phase of $cC_{\mathrm{rc}}\mathcal{M}_\perp$ is independent of the object and once it has been determined, one can exploit (9) and (11) or (10) and (11) to extract an estimate of ω even from a single image.

III. Inverting the MR Transform

In this section we study how one might design reconstruction algorithms that compute a discrete approximation to $\mathcal{M}^{-1}g$.

If $\mathcal{M}^{-1}$ were known explicitly, one could perhaps design a reconstruction algorithm by discretizing the formula for $\mathcal{M}^{-1}g$. Unfortunately, $\mathcal{M}^{-1}$ is not known in closed form. An alternative approach consists of computing a discrete version of $\mathcal{M}^{+}g$ where $\mathcal{M}^{+}$ is an explicitly known near inverse of $\mathcal{M}$.

One such near inverse is $\mathcal{F}^{-1}$. Approximating $\mathcal{M}^{-1}$ by $\mathcal{F}^{-1}$ is akin to the standard approach to MRI. To discuss the accuracy of this approach, we determine the point spread function (PSF) of the operator $\mathcal{F}^{-1}\mathcal{M} - \mathcal{I}$, i.e., the function P_0: $\mathbb{R}^2 \times \mathbb{R}^2 \to \mathbb{C}$ such that

$$(\mathcal{F}^{-1}\mathcal{M}f - f)(\mathbf{x}) = \int_{\mathbb{R}^2} P_0(\mathbf{x}, \mathbf{x}')h(\mathbf{x}')\,d\mathbf{x}'. \tag{29}$$

Using the explicit representations of $\mathcal{F}^{-1}$ and $\mathcal{M}$, one can easily show that P_0 is given by

$$P_0(\mathbf{x}, \mathbf{x}') = \frac{1}{(2\pi)^2}\int_{\mathbb{R}^2}\left(e^{-i\omega(\mathbf{x}')\tau(\mathbf{k})} - 1\right)e^{i(\mathbf{x}-\mathbf{x}')\cdot\mathbf{k}}\,d\mathbf{k}. \tag{30}$$

Inserting the series expansion

$$e^{-i\omega(\mathbf{x}')\tau(\mathbf{k})} - 1 = \sum_{l=1}^{\infty}\frac{i^l}{l!}\left(-\omega(\mathbf{x}')\tau(\mathbf{k})\right)^l \tag{31}$$

into the right-hand side (RHS) of (30) and interchanging the order of summation and integration gives

$$P_0(\mathbf{x}, \mathbf{x}') = \sum_{l=1}^{\infty}\frac{i^l}{l!}\left(-\omega(\mathbf{x}')\right)^l(\mathcal{F}^{-1}\tau^l)(\mathbf{x} - \mathbf{x}'). \tag{32}$$

The interchange is justified by the Lebesgue dominant convergence theorem [24], which is applicable because ω, τ, and the support of τ are bounded. Inspection of the RHS of (32) suggests that $P_0(\mathbf{x}, \mathbf{x}') \to 0$ as $|\mathbf{x} - \mathbf{x}'| \to \infty$. On the other

hand, when $\mathbf{x} \approx \mathbf{x}'$, then $|P_0(\mathbf{x}, \mathbf{x}')|$ will generally be small only in regions where $\omega \approx 0$. As a result, $\mathcal{F}^{-1}\mathcal{M}f$ will be close to f in regions where $|\omega|$ is small, but in regions where $|\omega|$ is not so small, $\mathcal{F}^{-1}\mathcal{M}f$ will generally not be close to f. While the influence of ω on P_0 is local, the influence of τ is nonlocal and more complicated. Still we can say that unless Ω or T are very small, $\mathcal{F}^{-1}$ is not a good approximation to $\mathcal{M}^{-1}$.

A much better approximation to $\mathcal{M}^{-1}$ is provided by the conjugate operator $\overline{\mathcal{M}} = \overline{\mathcal{M}}[\omega, \tau]$ given by the formula

$$(\overline{\mathcal{M}}g)(\mathbf{x}) = \frac{1}{(2\pi)^2} \int_{\mathbf{R}^2} g(\mathbf{k}) e^{i\omega(\mathbf{x})\tau(\mathbf{k})} e^{i\mathbf{x}\cdot\mathbf{k}}\, d\mathbf{k}. \tag{33}$$

The properties of $\overline{\mathcal{M}}$ are analogous to those of $\mathcal{M}$. Note that $\overline{\mathcal{M}} = \mathcal{F}^{-1}$ if $\omega = 0$. The PSF of $\overline{\mathcal{M}}\mathcal{M} - \mathcal{I}$ can be found like that of $\mathcal{F}^{-1}\mathcal{M} - \mathcal{I}$ and evaluates to

$$P_1(\mathbf{x}, \mathbf{x}') = \sum_{l=1}^{\infty} \frac{i^l}{l!} (\omega(\mathbf{x}) - \omega(\mathbf{x}'))^l (\mathcal{F}^{-1}\tau^l)(\mathbf{x} - \mathbf{x}'). \tag{34}$$

In contrast to P_0, this PSF depends on the difference between $\omega(\mathbf{x})$ and $\omega(\mathbf{x}')$. As a result, $\overline{\mathcal{M}}\mathcal{M}f$ will be close to f in regions where ω varies slowly, even if ω is not close to zero there. The influence of ω on P_1 is still local. If ω varies rapidly in some region, this will spoil the quality of the approximation only in that region. The influence of τ on P_1 is the same as that on P_0. We refer to computing $\overline{\mathcal{M}}g$ as conjugate phase reconstruction (CPR). This term was coined in [6] as an alias for the weighted correlation method proposed by Maeda *et al.* [26]. While the weighted correlation method was derived and analyzed in discrete terms, it may also be seen as a method for computing a discrete approximation to $\overline{\mathcal{M}}g$ by means of a matrix-vector product. However, since the matrix involved is dense and has $K^2 \times MN$ entries when the image has $K \times K$ pixels, the weighted correlation method is rather slow except for small images.

In Section IV we shall present a range of fast CPR algorithms. All these algorithms make use of an approximation of the form

$$e^{ist} \approx \sum_{l=0}^{L-1} c'_l(s) d'_l(t), \qquad s \in [\omega_-, \omega_+],\ t \in [\tau_-, \tau_+] \tag{35}$$

with suitable functions c'_l and d'_l. Substituting $\omega(\mathbf{x})$ for s and $\tau(\mathbf{k})$ for t and setting

$$c_l = c'_l \circ \omega, \qquad d_l = d'_l \circ \tau \tag{36}$$

turns (35) into

$$e^{i\omega(\mathbf{x})\tau(\mathbf{k})} \approx \sum_{l=0}^{L-1} c_l(\mathbf{x}) d_l(\mathbf{k}), \qquad \mathbf{x} \in \operatorname{supp} f,\ \mathbf{k} \in S. \tag{37}$$

Inserting (37) into (33) gives the approximation

$$\overline{\mathcal{M}}g \approx \sum_{l=0}^{L-1} c_l \mathcal{F}^{-1}(d_l g) \tag{38}$$

where we have also used the fact that the function $\overline{\mathcal{M}}g$ is sensitive to the values of $\omega(\mathbf{x})$ and $\tau(\mathbf{k})$ only when $\mathbf{x} \in \operatorname{supp} f$ (because $\overline{\mathcal{M}}g \approx f$ and the influence of ω is local) and when $\mathbf{k} \in S$ (because g was set to zero outside S).

A discrete version of the RHS of (38) can serve as a CPR algorithm. Different discretization strategies for the RHS of (38) or different functions c'_l and d'_l in (35) will lead to different CPR algorithms. Algorithms of this type can be arranged to take advantage of the fast Fourier transform (FFT), which makes them potentially faster than the weighted correlation method.

If ω_0 and τ_0 are arbitrary real constants, we obtain a variant of (38) by rewriting (33) as [cf. (26)]

$$\overline{\mathcal{M}}[\omega, \tau]g = e^{i\omega\tau_0} \overline{\mathcal{M}}[\omega - \omega_0, \tau - \tau_0] e^{i\omega_0(\tau - \tau_0)} g. \tag{39}$$

The expression on the right may be approximated similarly as the expression on the left, but now the approximation (35) needs to be good for $s \in [\omega_- - \omega_0, \omega_+ - \omega_0]$ and $t \in [\tau_- - \tau_0, \tau_+ - \tau_0]$.

Another interesting near inverse of $\mathcal{M}$ is given by $\mathcal{F}^{-1}\mathcal{M}_-\mathcal{F}^{-1}$ with $\mathcal{M}_- = \mathcal{M}[-\omega, \tau]$. Computing a discrete approximation to $\mathcal{F}^{-1}\mathcal{M}_-\mathcal{F}^{-1}g$ was proposed by Kadah and Hu under the name simulated phase evolution and rewinding (SPHERE) [9]. The PSF of $\mathcal{F}^{-1}\mathcal{M}_-\mathcal{F}^{-1}\mathcal{M}$ is analyzed in [9]. (Strictly speaking, the term SPHERE implies the usage of an estimate of ω obtained from two standard images in the usual way.)

In Section V we shall present a range of fast SPHERE algorithms. The essential step of these algorithms is the computation of $\mathcal{M}_- f_0$ with $f_0 = \mathcal{F}^{-1}g$. The approximation (37) now leads to

$$\mathcal{M}_- f_0 \approx \sum_{l=0}^{L-1} d_l \mathcal{F}(c_l f_0) \tag{40}$$

which is formally similar to (38).

A very accurate approximation to $\mathcal{M}^{-1}$ can be derived from the work of Norton [27]. Assuming that ω and τ are differentiable, this approximation reads

$$(\widetilde{\mathcal{M}}g)(\mathbf{x}) = \frac{1}{(2\pi)^2} \int_{\mathbf{R}^2} g(\mathbf{k}) |J_{\mathbf{T}_\mathbf{x}}(\mathbf{k})| e^{i\omega(\mathbf{x})\tau(\mathbf{k})} e^{i\mathbf{x}\cdot\mathbf{k}}\, d\mathbf{k} \tag{41}$$

where

$$J_{\mathbf{T}_\mathbf{x}}(\mathbf{k}) = 1 + \partial_1\tau(\mathbf{k})\, \partial_1\omega(\mathbf{x}) + \partial_2\tau(\mathbf{k})\, \partial_2\omega(\mathbf{x}) \tag{42}$$

is the Jacobian of the transformation $\mathbf{T}_\mathbf{x}$: $\mathbb{R}^2 \to \mathbb{R}^2$ defined by $\mathbf{T}_\mathbf{x}(\mathbf{k}) = \mathbf{k} + \tau(\mathbf{k})(\partial_1\omega(\mathbf{x}), \partial_2\omega(\mathbf{x}))$. It follows from (33), (41), and (42) that

$$\widetilde{\mathcal{M}}g = \overline{\mathcal{M}}g + \partial_1\omega\, \overline{\mathcal{M}}(g\partial_1\tau) + \partial_2\omega\, \overline{\mathcal{M}}(g\partial_2\tau). \tag{43}$$

Thus, computing $\widetilde{\mathcal{M}}g$ can be reduced to three CPR's. Ignoring the derivative terms in (43) leads back to ordinary CPR.

Whenever we know a good near inverse of $\mathcal{M}$, we can compute $\mathcal{M}^{-1}g$ iteratively [28, Sec. 2.5]. With $\overline{\mathcal{M}}$ as near inverse, the iteration reads

$$f_1 = \overline{\mathcal{M}}g \tag{44}$$

$$f_{n+1} = f_n + \overline{\mathcal{M}}(g - \mathcal{M}f_n), \qquad n = 1, 2, \ldots. \tag{45}$$

The initial step once again amounts to ordinary CPR. Each subsequent step requires one CPR and one evaluation of $\mathcal{M}f_n$. This term may be computed similarly as $\mathcal{M}_- f_0$ in

(40). Convergence is guaranteed if $\|\mathcal{I} - \overline{\mathcal{M}}\mathcal{M}\| < 1$, where $\|\cdot\|$ denotes the operator norm in $L_2(\mathbb{R}^2)$. We refer to the algorithm (44), (45) as CPR with post-iteration. The algorithms presented in Sections IV and V may also be used to implement CPR with post-iteration.

A different class of algorithms for computing $h = \mathcal{M}^{-1}g$ is obtained by discretizing the equation $\mathcal{M}h = g$ and solving the resulting linear systems of equations. It is also possible to solve a discrete version of the equivalent equation $\mathcal{F}^{-1}\mathcal{P}h + h = \mathcal{F}^{-1}g$, which is a Fredholm integral equation of the second kind for h [29]. Methods of this kind are described in [30]. It seems, however, that the resulting algorithms are slower than the algorithms presented in this paper.

IV. Fast CPR Algorithms

A. Preliminaries

From now on we assume that f has its support in $R_\square(Kd/2)$ for some (large) integer K and some (small) number $d > 0$. For simplicity, K is to be an "FFT-friendly" integer that admits an FFT algorithm. We also assume that S is a subset of $S_\square(\pi/d)$. The grid formed by the sampling points $\mathbf{p}_m(t_n)$ need not be Cartesian and, unless stated otherwise, we assume that it is not. We can compute a standard image on a $K \times K$ Cartesian grid in $R_\square(Kd/2)$ with grid spacing d using the gridding method [31]–[33]. The procedure may be formulated as

$$\mathbf{f}_0 = \mathbf{v}\boldsymbol{\mathcal{F}}_{\mathrm{FFT}}^{-1}\boldsymbol{\mathcal{C}}\mathbf{s} \tag{46}$$

where $\mathbf{s} \in \mathbb{C}^{MN}$ is the vector with components $g(\mathbf{p}_m(t_n)) = s_m(t_n)$, $\boldsymbol{\mathcal{C}}$ a discrete convolution operator, $\boldsymbol{\mathcal{F}}_{\mathrm{FFT}}^{-1}$ an FFT-based discrete version of $\mathcal{F}^{-1}$, $\mathbf{v} \in \mathbb{R}^{KK}$ a discrete weighting function, and $\mathbf{f}_0 \in \mathbb{C}^{KK}$ the resulting standard image. We regard the vectors occurring in (46) as "grid functions" and $\boldsymbol{\mathcal{C}}$ and $\boldsymbol{\mathcal{F}}_{\mathrm{FFT}}^{-1}$ as operators acting on grid functions. Specifically, the operator $\boldsymbol{\mathcal{C}}$ transforms $\mathbf{s}$, which is a discrete approximation to g on the non-Cartesian grid in S, into a discrete approximation to $w * g$ on a $K \times K$ Cartesian grid in $S_\square(\pi/d)$ with grid spacing $2\pi/(dK)$ where w is an auxiliary window function with a small support. The operator $\boldsymbol{\mathcal{F}}_{\mathrm{FFT}}^{-1}$ transforms the output of this "gridding step" into a discrete approximation to $\mathcal{F}^{-1}(w * g) = (2\pi)^2(\mathcal{F}^{-1}w)(\mathcal{F}^{-1}g)$ on the Cartesian grid in $R_\square(Kd/2)$. The grid function $\mathbf{v}$ is a discrete approximation to $(2\pi)^{-2}(\mathcal{F}^{-1}w)^{-1}$ on the same grid. The juxtaposition of $\mathbf{v}$ and $\boldsymbol{\mathcal{F}}_{\mathrm{FFT}}^{-1}\boldsymbol{\mathcal{C}}\mathbf{s}$ in (46) is understood as pointwise multiplication.

Finally, we assume that the region S is so large and the sampling pattern in S so dense that the standard image is not seriously degraded by truncation and aliasing errors. Also, the errors in the data and the off-resonance effect should be so small that the standard image is at least a crude approximation of f.

We wish to compute a grid function $\mathbf{f} \in \mathbb{C}^{KK}$ that is a discrete approximation to the RHS of (38) (or its variant for $\overline{\mathcal{M}}[\omega - \omega_0, \tau - \tau_0]$) on the Cartesian grid in $R_\square(Kd/2)$. An estimate of the frequency map is needed on the same Cartesian grid. Also needed is a safe estimate R_0 of the support of f. If the standard image is available and not too degraded, it may be used to find an R_0 that is only a little larger than $\operatorname{supp} f$. In the worst case, $R_0 = R_\square(Kd/2)$ may have to be chosen. The available estimates of $\operatorname{supp} f$ and ω are then used to estimate the numbers ω_-, ω_+, and Ω defined in (7) and (8). For simplicity, we shall use the symbols ω_-, ω_+, and Ω also for the respective estimates. The time map may or may not be known in closed form.

B. Discretization Strategies

First we discuss three discretization strategies for the RHS of (38) (or one of its variants), assuming that the integer L and the functions c_l' and d_l' in (35) and (36) have already been chosen. Each discretization strategy leads to a different class of algorithms.

The critical step is the discretization of the terms $\mathcal{F}^{-1}(d_l g)$. Since the functions $d_l = d_l' \circ \tau$ and g are certainly known on the non-Cartesian grid in $S_\square(\pi/d)$, we may use the gridding method to compute $\mathcal{F}^{-1}(d_l g)$. The resulting algorithms have the general form

$$\mathbf{f} = \mathbf{v}\sum_{l=0}^{L-1} \mathbf{c}_l \boldsymbol{\mathcal{F}}_{\mathrm{FFT}}^{-1}\boldsymbol{\mathcal{C}}(\tilde{\mathbf{d}}_l\mathbf{s}). \tag{47}$$

Here, $\tilde{\mathbf{d}}_l \in \mathbb{C}^{MN}$ is a discrete version of d_l, sampled on the non-Cartesian grid in $S_\square(\pi/d)$, and $\mathbf{c}_l \in \mathbb{C}^{KK}$ is a discrete version of c_l, sampled on the Cartesian grid in $R_\square(Kd/2)$. Again, the juxtaposition of two grid functions on the same grid in (47) is understood as pointwise multiplication. The summation in (47) is also understood pointwise. (These conventions also apply to similar formulas below.) Since $d_l(\mathbf{p}_m(t_n)) = d_l'(\tau(\mathbf{p}_m(t_n))) = d_l'(t_n)$, the time map is not explicitly needed. CPR algorithms based on this discretization strategy were proposed by Noll *et al.* [6], [7].

To avoid all but one of the time consuming gridding steps, Man *et al.* [8] suggested replacing $\boldsymbol{\mathcal{C}}(\tilde{\mathbf{d}}_l\mathbf{s})$ in (47) by $\mathbf{d}_l\boldsymbol{\mathcal{C}}\mathbf{s}$, where $\mathbf{d}_l \in \mathbb{C}^{KK}$ is a discrete version of d_l sampled on the Cartesian grid in $S_\square(\pi/d)$. The resulting algorithms have the general form

$$\mathbf{g}^* = \boldsymbol{\mathcal{C}}\mathbf{s} \tag{48}$$

$$\mathbf{f} = \mathbf{v}\sum_{l=0}^{L-1} \mathbf{c}_l \boldsymbol{\mathcal{F}}_{\mathrm{FFT}}^{-1}(\mathbf{d}_l\mathbf{g}^*). \tag{49}$$

It is now necessary to evaluate $d_l = d_l' \circ \tau$ on the Cartesian grid in $S_\square(\pi/d)$. This is no problem if τ is known in closed form. Otherwise, some form of interpolation must be used to resample τ or d_l from the non-Cartesian grid to the Cartesian grid in $S_\square(\pi/d)$. If the time map is discontinuous in S, this interpolation may incur an extra error.

The replacement of $\boldsymbol{\mathcal{C}}(\tilde{\mathbf{d}}_l\mathbf{s})$ by $\mathbf{d}_l\boldsymbol{\mathcal{C}}\mathbf{s}$ creates some error, too. As the gridding step is, in essence, a discrete version of a convolution with a narrow window function, this error is negligible when d_l is smooth. However, d_l is not always smooth. For example, the natural time maps of spiral and radial MRI (cf. Section VI) are not differentiable at $\mathbf{k} = 0$ and this behavior carries over to d_l. Some time maps are even discontinuous in S.

To avoid this extra error, we suggest resampling $\mathbf{s}$ onto the Cartesian grid in $S_{\square}(\pi/d)$ by first computing $\mathbf{f}_0$ via (46) and then

$$\mathbf{g} = \boldsymbol{\mathcal{F}}_{\mathrm{FFT}}\mathbf{f}_0 \tag{50}$$

$$\mathbf{f} = \sum_{l=0}^{L-1} \mathbf{c}_l \boldsymbol{\mathcal{F}}_{\mathrm{FFT}}^{-1}(\mathbf{d}_l \mathbf{g}). \tag{51}$$

In (50), $\boldsymbol{\mathcal{F}}_{\mathrm{FFT}}$ represents an FFT-based discrete version of $\mathcal{F}$. Together, (46) and (50) effect a resampling of the MR data from the non-Cartesian grid to the Cartesian grid in $S_{\square}(\pi/d)$ [33]. The general algorithm (50), (51) acts on the standard image and involves only Cartesian grids. When combined with (46), it requires two 2-D FFT's more than the general algorithm (48), (49). In many situations, the standard image is already available or needs to be computed anyway, and then the extra cost reduces to a single 2-D FFT. If τ is continuous in S, then $\mathcal{M}f$ will also be continuous there and the resampling of g via (46) and (50) will be accurate. Conversely, if τ is discontinuous in S, then $\mathcal{M}f$ will also be discontinuous there and the resampling may of g be inaccurate.

Discontinuous time maps (on non-Cartesian grids) remain difficult to cope with. In the case of ring-segmented spiral MRI or other segmented non-Cartesian MRI methods, one can still apply an instantiation of one of the general algorithms (48) and (49) or (50) and (51) to the data in each segment separately and add the results. If there are many segments, algorithms based on (47) may be faster.

C. The Algorithms

We now discuss possible choices for the functions c_l' and d_l' in (35). In principle, each choice can be combined with any of the three discretization strategies described in Section IV-B. The CPR algorithms presented in this paper, however, are all based on (50) and (51).

In practice, one also needs some way of estimating the number of terms, L, from the data. For the moment, we suggest choosing L via a parameter $\beta > 0$ in the form

$$L = \lceil \beta \Omega T/(2\pi) \rceil \tag{52}$$

the hope being that β might become an algorithm-dependent constant.

1) Discrete Frequency Exponential Approximation: A natural choice for the functions d_l', proposed by Noll *et al.* [7], are the discrete frequency exponentials

$$d_l'(t) = e^{i\omega_l t}, \qquad 0 \le l < L. \tag{53}$$

The frequencies ω_l and the companion functions c_l' are yet to be determined.

One of the simplest choices for ω_l and c_l', also indicated in [7], is

$$\omega_l = \omega_- + \left(l + \tfrac{1}{2}\right)\Omega/L, \qquad 0 \le l < L \tag{54}$$

$$c_l'(s) = \begin{cases} 1, & \text{if } -\dfrac{\Omega}{2L} \le s - \omega_l < \dfrac{\Omega}{2L} \\ 0, & \text{else.} \end{cases} \tag{55}$$

The associated functions $c_l = c_l' \circ \omega$ are discontinuous and define a partitioning of R_0 into the disjoint segments

$$\tilde{R}_l = \{\mathbf{x} \in R_0 \,|\, c_l(\mathbf{x}) = 1\}. \tag{56}$$

The effect of the choice (55) is a sort of nearest neighbor interpolation in (51). The algorithm (50), (51) with d_l' as in (53), ω_l as in (54), and c_l' as in (55), will be referred to as algorithm CPR-DFE-NN. (DFE stands for discrete frequency exponential approximation, NN for nearest neighbor interpolation.)

The image quality offered by algorithm CPR-DFE-NN may be hampered by the discontinuity of the functions c_l. (Spiral MRI is an important exception, see Sections VI and VII). The following choice, due to Man *et al.* [8], avoids this problem. Let $\beta_1 > 1$ and $\beta_2 > 1$ be two parameters subject to

$$L = \beta_1 \beta_2 \Omega T/(2\pi). \tag{57}$$

Also let

$$\omega_{\mathrm{c}} = (\omega_- + \omega_+)/2, \qquad \Omega_\pm = \omega_{\mathrm{c}} \pm \beta_1 \Omega/2 \tag{58}$$

$$\Delta\omega = \beta_1 \Omega/L, \quad \omega_l = \Omega_- + \left(l + \tfrac{1}{2}\right)\Delta\omega, \qquad 0 \le l < L. \tag{59}$$

Similarly, let

$$\tau_{\mathrm{c}} = (\tau_- + \tau_+)/2, \qquad T_\pm = \tau_{\mathrm{c}} \pm \beta_2 T/2 \tag{60}$$

$$\Delta\tau = \beta_2 T/L, \qquad \tau_k = T_- + \left(k + \tfrac{1}{2}\right)\Delta\tau, \quad 0 \le k < L. \tag{61}$$

Then for each $s \in [\omega_-, \omega_+]$ define ε_s: $[T_-, T_+] \to \mathbb{C}$ by

$$\varepsilon_s(t) = w(t) e^{ist} \tag{62}$$

where w: $[T_-, T_+] \to \mathbb{R}$ is a window function such as

$$w(t) = \begin{cases} \cos^2\left(\dfrac{\pi}{2}\,\dfrac{t - \tau_-}{T_- - \tau_-}\right), & \text{if } T_- \le t < \tau_- \\ 1, & \text{if } \tau_- \le t \le \tau_+ \\ \cos^2\left(\dfrac{\pi}{2}\,\dfrac{t - \tau_+}{T_+ - \tau_+}\right), & \text{if } \tau_+ < t \le T_+. \end{cases} \tag{63}$$

Note that $\varepsilon_s(t) = e^{ist}$ when $t \in [\tau_-, \tau_+]$. For each $s \in [\omega_-, \omega_+]$ we wish to approximate ε_s in $[T_-, T_+]$ by a trigonometric polynomial of the form

$$\Pi_s(t) = \sum_{l=0}^{L-1} c_l'(s) e^{i\omega_l t}, \qquad t \in [T_-, T_+]. \tag{64}$$

Suitable coefficients $c_l'(s)$ can be found by trigonometric interpolation, i.e., by requesting that

$$\varepsilon_s(\tau_k) = \Pi_s(\tau_k), \qquad 0 \le k < L. \tag{65}$$

In view of (57)–(62) and (64), this may be rewritten as

$$\varepsilon_s(\tau_k) e^{-i\omega_0 \tau_k} = \sum_{l=0}^{L-1} c_l'(s) e^{il\Delta\omega\tau_0} e^{i2\pi kl/L}, \qquad 0 \le k < L. \tag{66}$$

The coefficients $c_l'(s)$ are then given by [34]

$$c_l'(s) = \frac{e^{-il\Delta\omega\tau_0}}{L} \sum_{k=0}^{L-1} \varepsilon_s(\tau_k) e^{-i\omega_0\tau_k} e^{-i2\pi kl/L} \qquad 0 \le l < L. \quad (67)$$

In practice, one calculates the coefficients $c_l'(s)$ for a finely spaced set of frequencies $s_j \in [\omega_-, \omega_+]$ and uses interpolation to find them at intermediate values of s. It can be deduced from (67) that

$$c_l'(s+\Delta\omega) = c_{l-1}'(s), \qquad 1 \le l < L \quad (68)$$

$$c_0'(s+\Delta\omega) = e^{-iL\Delta\omega\tau_0} c_{L-1}'(s). \quad (69)$$

It therefore suffices to compute $c_l'(s_j)$ only for the s_j in one of the frequency bins $[\omega_l, \omega_{l+1}]$. Unless L happens to be FFT-friendly, the sum (67) cannot be evaluated via an FFT but, in practice, L is so small that a direct evaluation via (67) is fairly fast. To achieve a good approximation in (35) with a small L, the choice of β_1 and β_2 is both essential and critical (cf. Section VII). The algorithm (50), (51), with d_l' as in (53), ω_l as in (59), and c_l' as in (67), will be referred to as CPR-DFE-T. (T stands for trigonometric interpolation.)

2) Discrete Time Exponential Approximation: We obtain dual algorithms if we interchange the roles of s and t. The functions c_l' are then discrete time exponentials,

$$c_l'(s) = e^{is\tau_l}, \qquad 0 \le l < L \quad (70)$$

and the times τ_l and the companion functions d_l' are still to be determined. If we choose them in analogy to (54) and (55), we obtain algorithm CPR-DTE-NN (DTE stands for discrete time exponential approximation.) A version of algorithm CPR-DTE-NN based on (47) was proposed by Noll *et al.* [6]. The analogs of the choices (57)–(67) lead to algorithm CPR-DTE-T.

3) Polynomial Approximation: It was pointed out in [8] that the functions d_l' might also be chosen as polynomials in t, although suitable companion functions c_l' were not exhibited. It was also demonstrated that discrete frequency exponentials are nearly optimal. Nevertheless, polynomial approximation can lead to an attractive CPR algorithm, as we shall now show.

The algorithm to be presented turns out to be fastest when it works with centered versions of ω and τ. These are defined by

$$\tilde\omega = \omega - \omega_c, \qquad \tilde\tau = \tau - \tau_c \quad (71)$$

with ω_c and τ_c as in (58) and (60), respectively. With the further definitions

$$\overline{\mathcal{M}}_c = \overline{\mathcal{M}}[\omega_c, \tau_c], \qquad \tilde g = e^{i\omega_c\tilde\tau} g \quad (72)$$

we have

$$\overline{\mathcal{M}} g = e^{i\omega\tau_c} \overline{\mathcal{M}}_c \tilde g \quad (73)$$

as a special case of (39). Due to the centering, we further have $\tilde\omega(\mathbf{x}) \in [-\Omega/2, \Omega/2]$ if $\mathbf{x} \in R_0$ and $\tilde\tau(\mathbf{k}) \in [-T/2, T/2]$ if $\mathbf{k} \in S$. As a result, we now need to find functions c_l' such that

$$e^{ist} \approx \sum_{l=0}^{L-1} c_l'(s) t^l, \qquad s \in [-\Omega/2, \Omega/2],\ t \in [-T/2, T/2]. \quad (74)$$

We propose to let $c_l'(s) = (a_l + ib_l)s^l$ with real coefficients a_l and b_l yet to be determined. This choice makes the function $c_l'(s)t^l$ a polynomial in the single variable $\phi = st$. Moreover, due to the centering, $\phi \in [-\Omega T/4, \Omega T/4]$ when $s \in [-\Omega/2, \Omega/2]$ and $t \in [-T/2, T/2]$. So now we seek real coefficients a_l and b_l such that

$$e^{i\phi} \approx \sum_{l=0}^{L-1} (a_l + ib_l)\phi^l, \qquad \phi \in [-\Omega T/4, \Omega T/4]. \quad (75)$$

To find such coefficients, we determine the real polynomial $p(\phi) = \sum_{l=0}^{L-1} a_l\phi^n$ that interpolates the function $\Re e^{i\phi} = \cos\phi$ at the L zeroes of the transformed Chebyshev polynomial $\tilde T_L(\phi) = T_L(\xi(\phi))$ in the interval $[-\Omega T/4, \Omega T/4]$, where T_L is the standard Chebyshev polynomial of degree L and $\xi(\phi) = (\phi + \Omega T/4)/(\Omega T) - 1$. The polynomial $p(\phi)$ is easy to compute and affords nearly the same accuracy in $[-\Omega T/4, \Omega T/4]$ as the minimax polynomial of the same degree [28, Secs. 5.8–5.10]. The coefficients b_l are found similarly by interpolating $\Im e^{i\phi} = \sin\phi$. Since the interval $[-\Omega T/4, \Omega T/4]$ is centered and the function $\cos\phi$ is even, the coefficients a_l are zero when l is odd. Similarly, the coefficients b_l are zero when l is even. The number of terms required to achieve a prescribed accuracy in (75) increases with the size of the interval in which the approximation must be good. Centering ω and τ minimizes the size of this interval and also centers it.

The resulting algorithm may be stated as follows:

$$\tilde{\mathbf{g}} = e^{i\omega_c\tilde{\boldsymbol\tau}} \boldsymbol{\mathcal{F}}_{\mathrm{FFT}} \mathbf{f}_0 \quad (76)$$

$$\tilde{\mathbf{f}}_{\mathrm{e}} = \sum_{l=0}^{\lfloor (L-1)/2 \rfloor} a_{2l} \tilde{\boldsymbol\omega}^{2l} \boldsymbol{\mathcal{F}}_{\mathrm{FFT}}^{-1}(\tilde{\boldsymbol\tau}^{2l} \tilde{\mathbf{g}}) \quad (77)$$

$$\tilde{\mathbf{f}}_{\mathrm{o}} = \sum_{l=1}^{\lceil (L-1)/2 \rceil} b_{2l-1} \tilde{\boldsymbol\omega}^{2l-1} \boldsymbol{\mathcal{F}}_{\mathrm{FFT}}^{-1}(\tilde{\boldsymbol\tau}^{2l-1} \tilde{\mathbf{g}}) \quad (78)$$

$$\mathbf{f} = e^{i\boldsymbol\omega\tau_c}(\tilde{\mathbf{f}}_{\mathrm{e}} + i\tilde{\mathbf{f}}_{\mathrm{o}}). \quad (79)$$

Here, $e^{i\omega_c\tilde{\boldsymbol\tau}}$, $\tilde{\boldsymbol\omega}$, $\tilde{\boldsymbol\tau}$, and $e^{i\boldsymbol\omega\tau_c}$ are discrete versions of the functions $e^{i\omega_c\tilde\tau}$, $\tilde\omega$, $\tilde\tau$, and $e^{i\omega\tau_c}$, respectively, sampled on the pertinent Cartesian grids. The algorithm (76)–(79) with the above choice of the coefficients will be referred to as algorithm CPR-P (P stands for polynomial approximation).

For large values of L and ΩT, the summations and multiplications in (77) and (78) involve numbers of grossly different orders of magnitude. In such cases, algorithm CPR-P may suffer from a loss of accuracy due to rounding errors.

Interchanging the roles of s and t in (74) does not lead to a new algorithm.

D. Miscellaneous Remarks

The accuracy of the above algorithms depends on the accuracy of the approximation in (35) or (75). This accuracy, in turn, depends on the choice of the functions c_l' and d_l' and will generally increase with L. The number of terms necessary to achieve a prescribed accuracy will also grow with ΩT. Different algorithms may well produce different artifacts. The accuracy of the resulting images will also be affected by the accuracy of the available frequency map.

The computational effort for computing one of the terms in the sums (51) or (77) and (78) is dominated by the effort for computing a 2-D complex FFT. Thus, the computational complexity of these algorithms is mainly determined by the number of terms required for the desired accuracy. The operation count may be reduced a little by means of a binary mask indicating the region R_0. Such a mask is also useful to suppress artifacts that may arise when the estimated frequency map is grossly false and nonzero outside R_0.

In principle, the CPR algorithms presented in Section IV-C may be applied to Cartesian MRI as well. The initial resampling of the MR data onto a Cartesian grid in $S_\square(\pi/d)$ is then unnecessary. Also, there is no need to resample the time map when it is not known in closed form. The standard image will be distorted and, if the frequency map is obtained in the usual way, it will be distorted as well. Algorithm CPR-DFE-NN is not usable with Cartesian MRI, as it shifts the segments $\tilde{R}_l$ defined in (56) by different amounts, thus leaving the boundaries between the segments visible. The fact that the time map of a Cartesian MRI method depends only on k_1 (or k_2), may be used to speed up the computation of the 2-D FFT's involved.

V. Fast SPHERE Algorithms

Every CPR algorithm presented in Section IV-C has a SPHERE counterpart. The general form of these algorithms is [cf. (40)]

$$\mathbf{h} = \sum_{l=0}^{L-1} \mathbf{d}_l \mathcal{F}_{\mathrm{FFT}}(\mathbf{c}_l \mathbf{f}_0) \tag{80}$$

$$\mathbf{f} = \mathcal{F}_{\mathrm{FFT}}^{-1}\mathbf{h}. \tag{81}$$

Like the CPR algorithms of Section IV-C, these algorithms act on $\mathbf{f}_0$ and work with Cartesian grids throughout. The functions c_l' and d_l' may be chosen in the same way as in Section IV-C. Specifically, if d_l', ω_l, and c_l' are chosen as in (53)–(55), respectively, we obtain algorithm SPH-DFE-NN, the SPHERE counterpart of CPR-DFE-NN. Algorithms SPH-DFE-T, SPH-DTE-NN, SPH-DTE-T, and SPH-P arise similarly. Algorithm SPH-DFE-NN leaves the boundaries between the segments $\tilde{R}_l$ defined in (56) visible and is not usable. Algorithm SPH-DTE-NN was first described in [9].

Assuming the same number of terms, the computational complexity of all these SPHERE algorithms is similar to that of their CPR counterparts. Most remarks made in Section IV-D carry over.

After a change of the sign of ω and without the final inverse Fourier transformation, these SPHERE algorithms are also suited to compute the term $\mathcal{M}f_n$ in (45).

VI. Application to Spiral MRI

The trajectories of spiral MRI [18]–[20] are interleaved archimedian spirals covering the disk $S_\circ(\pi/d)$. The trajectories may be written as

$$\mathbf{p}_m(t) = (\Re\sigma_m(\psi((t-\tau_-)/T)), \Im\sigma_m(\psi((t-\tau_-)/T))), \quad 0 \le m < M,\ t \in [\tau_-, \tau_+] \tag{82}$$

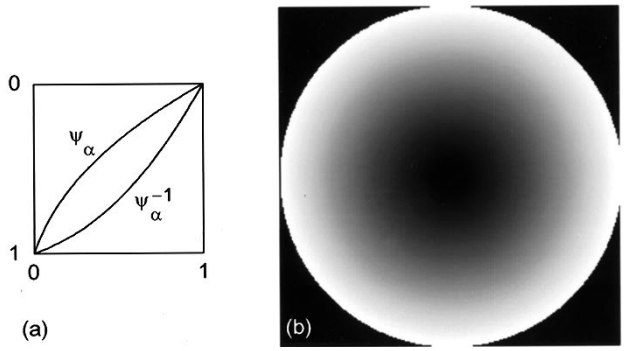

Fig. 1. (a) The function ψ_α defined in (85) and its inverse, ψ_α^{-1}. In this example, $\alpha = 0.125$. (b) The associated time map, as defined in (84).

where σ_m: $[0, 1] \to \mathbb{C}$ is defined by

$$\sigma_m(s) = (\pi/d)se^{i2\pi Ks/(2M)}e^{i2\pi m/M} \tag{83}$$

and ψ: $[0, 1] \to [0, 1]$ is a smooth monotonically increasing function with $\psi(0) = 0$ and $\psi(1) = 1$. The natural time map is

$$\tau(\mathbf{k}) = \begin{cases} T\psi^{-1}(d|\mathbf{k}|/\pi), & \text{if } \mathbf{k} \in S_\circ(\pi/d) \\ 0, & \text{else.} \end{cases} \tag{84}$$

A good choice for ψ is [5, Sec. 3.6]

$$\psi_\alpha(u) = \frac{u}{\sqrt{\alpha + (1-\alpha)u}}, \qquad 0 < \alpha \ll 1 \tag{85}$$

in which case the sampling density in $S_\circ(\pi/d)$ is adequate when $MN \ge (\pi/4)K^2$. Fig. 1(a) illustrates the functions ψ_α and ψ_α^{-1} for $\alpha = 0.125$. Fig. 1(b) shows the resulting natural time map.

The functions τ^l and $\mathcal{F}^{-1}\tau^l$ are real and rotationally symmetric. In regions where ω varies slowly, the rotational symmetry of $\mathcal{F}^{-1}\tau^l$ shapes the PSF (32) of $\mathcal{F}^{-1}\mathcal{M} - \mathcal{I}$ in a way that makes $\mathcal{F}^{-1}\mathcal{M}f$ a blurred version of f, where the amount of blur near $\mathbf{x}$ grows with $|\omega(\mathbf{x})|$ and T. The blurring of the standard image makes it possible to obtain a good yet safe estimate of $\operatorname{supp} f$.

The algorithms described in Sections IV and V may be used to deblur standard spiral MRI images. Despite the discontinuity of its coefficient functions, algorithm CPR-DFE-NN is applicable to spiral MRI, because the small amount of remaining blur tends to obscure the boundaries between the segments $\tilde{R}_l$ defined in (56).

Furthermore, algorithm CPR-P may be speeded up considerably, provided ω and the phase of f are reasonably smooth (which they usually are). We can formulate the requirement for f as

$$f = e^{i\phi}r = e^{i\phi}(r_{\mathrm{lo}} + r_{\mathrm{hi}}) \tag{86}$$

where the functions ϕ, r, r_{lo}, and r_{hi} are real $r \ge 0$ and

$$e^{i\phi}r_{\mathrm{lo}} = \mathcal{F}^{-1}(w_{\mathrm{lo}}\mathcal{F}f) \tag{87}$$

for some low-pass filter w_{lo}, such as

$$w_{\mathrm{lo}}(\mathbf{k}) = \cos^2(\alpha_1\, d|\mathbf{k}|/2), \qquad 0 < \alpha_1 \ll 1. \tag{88}$$

For the fast version of algorithm CPR-P, let ω_c, τ_c, $\tilde{\omega}$, $\tilde{\tau}$, and $\overline{\mathcal{M}}_c$ be defined as in Section IV-C-3. The algorithm exploits the fact that the function

$$\tilde{h} = \mathcal{F}(e^{-i(\phi-\omega_c\tau_c)}e^{i\tilde{\omega}\tau_c}\mathcal{F}^{-1}(e^{i\omega_c\tilde{\tau}}g)) \tag{89}$$

is computable from g and satisfies

$$\overline{\mathcal{M}}_c\tilde{h} \approx r. \tag{90}$$

We first show that $\tilde{h}$ is computable from g. Since $\tau(\mathbf{k}) \approx 0$ near the origin of $\mathbf{k}$ space, we have

$$\begin{aligned}\mathcal{F}^{-1}(w_{\mathrm{lo}}e^{i\omega_c\tilde{\tau}}g) &\approx \mathcal{F}^{-1}(w_{\mathrm{lo}}e^{i\omega_c\tilde{\tau}}\mathcal{M}f) &(91)\\ &\approx e^{-i\omega_c\tau_c}\mathcal{F}^{-1}(w_{\mathrm{lo}}(\mathcal{F}f)) &(92)\\ &= e^{i(\phi-\omega_c\tau_c)}r_{\mathrm{lo}}. &(93)\end{aligned}$$

So $e^{i(\phi-\omega_c\tau_c)}$ is computable from g. All other terms in (89) are either known or also computable.

To demonstrate (90), we note that

$$\begin{aligned}\overline{\mathcal{M}}_c\tilde{h} &= e^{-i\tilde{\omega}\tau_c}\overline{\mathcal{M}}(e^{-i\omega_c\tau}\tilde{h}) &(94)\\ &= e^{-i\tilde{\omega}\tau_c}\overline{\mathcal{M}}(e^{-i\omega_c\tau}\mathcal{F}(e^{-i\phi}e^{i\omega\tau_c}\mathcal{F}^{-1}(e^{i\omega_c\tilde{\tau}}g))) &(95)\\ &\approx e^{-i\phi}e^{i\omega\tau_c}e^{-i\tilde{\omega}\tau_c}\overline{\mathcal{M}}(e^{-i\omega_c\tau}e^{i\omega_c\tilde{\tau}}g) &(96)\\ &= e^{-i\phi}\overline{\mathcal{M}}g &(97)\\ &\approx r. &(98)\end{aligned}$$

The crucial step here is the transition from (95) to (96), which is based on an interchange of the order of the multiplication with $e^{-i\phi}e^{i\omega\tau_c}$ and the application of the operator $\overline{\mathcal{M}}e^{-i\omega_c\tau}\mathcal{F}$. The error resulting from this interchange is small because $e^{-i\phi}e^{i\omega\tau_c}$ is smooth by assumption and the PSF of $\overline{\mathcal{M}}e^{-i\omega_c\tau}\mathcal{F} - \mathcal{I}$

$$\begin{aligned}\tilde{P}_0(\mathbf{x},\mathbf{x}') &= \frac{1}{(2\pi)^2}\int_{\mathbb{R}^2}\left(e^{i\tilde{\omega}(\mathbf{x})\tau(\mathbf{k})}-1\right)e^{i(\mathbf{x}-\mathbf{x}')\cdot\mathbf{k}}\,d\mathbf{k} &(99)\\ &= \sum_{l=1}^{\infty}\frac{i^l}{l!}\,\tilde{\omega}^l(\mathbf{x})(\mathcal{F}^{-1}\tau^l)(\mathbf{x}-\mathbf{x}') &(100)\end{aligned}$$

is concentrated where $\mathbf{x} \approx \mathbf{x}'$.

Now we show that $\overline{\mathcal{M}}_c\tilde{h}$ can be computed efficiently. Like any other complex-valued function, $\tilde{h}$ admits the representation

$$\tilde{h} = \tilde{h}_1 + i\tilde{h}_2 \tag{101}$$

with the Hermitian functions

$$\tilde{h}_1 = \mathcal{F}(\Re(\mathcal{F}^{-1}\tilde{h})), \qquad \tilde{h}_2 = \mathcal{F}(\Im(\mathcal{F}^{-1}\tilde{h})). \tag{102}$$

Exactly as described in Section IV-C3, we can find an integer $L \geq 0$ and real coefficients a_l, b_l such that $a_l = 0$ when l is odd, $b_l = 0$ when l is even, and

$$\overline{\mathcal{M}}_c\tilde{h} \approx \sum_{l=0}^{L-1}(a_l + ib_l)\tilde{\omega}^l\mathcal{F}^{-1}(\tilde{\tau}^l\tilde{h}). \tag{103}$$

Substituting (101) into the RHS of (103) gives

$$\overline{\mathcal{M}}_c\tilde{h} \approx r_{\mathrm{e},1} + ir_{\mathrm{e},2} + ir_{\mathrm{o},1} - r_{\mathrm{o},2} \tag{104}$$

with

$$r_{\mathrm{e,k}} = \sum_{l=0}^{\lfloor (L-1)/2\rfloor} a_{2l}\tilde{\omega}^{2l}\mathcal{F}^{-1}(\tilde{\tau}^{2l}\tilde{h}_k), \qquad k = 1, 2 \tag{105}$$

$$r_{\mathrm{o,k}} = \sum_{l=1}^{\lceil (L-1)/2\rceil} b_{2l-1}\tilde{\omega}^{2l-1}\mathcal{F}^{-1}(\tilde{\tau}^{2l-1}\tilde{h}_k), \qquad k = 1, 2. \tag{106}$$

The functions $r_{\mathrm{e,k}}$ and $r_{\mathrm{o,k}}$ are real because the coefficients a_{2l} and b_{2l-1} are real, $\tilde{\omega}$ is real, $\tilde{h}_1$ and $\tilde{h}_2$ are Hermitian, and $\tilde{\tau}$ is real and rotationally symmetric (and hence Hermitian). Since $\overline{\mathcal{M}}_c\tilde{h}$ must be nearly real, $r_{\mathrm{e},2}$ and $r_{\mathrm{o},1}$ must be nearly zero and

$$\overline{\mathcal{M}}_c\tilde{h} \approx r_{\mathrm{e},1} - r_{\mathrm{o},2}. \tag{107}$$

Combining all these observations leads to the following algorithm for computing a discrete approximation $\mathbf{r}$ to $r = |f|$ from $\mathbf{f}_0$:

$$\begin{aligned}\tilde{\mathbf{g}} &= e^{i\omega_c\tilde{\boldsymbol{\tau}}}\boldsymbol{\mathcal{F}}_{\mathrm{FFT}}\mathbf{f}_0 &(108)\\ \tilde{\mathbf{f}}_{\mathrm{lo}} &= \boldsymbol{\mathcal{F}}^{-1}_{\mathrm{FFT}}(\mathbf{w}_{\mathrm{lo}}\tilde{\mathbf{g}}) &(109)\\ \tilde{\mathbf{r}} &= e^{i\tilde{\boldsymbol{\omega}}\tau_c}\overline{\tilde{\mathbf{f}}_{\mathrm{lo}}}|\tilde{\mathbf{f}}_{\mathrm{lo}}|^{-1}\boldsymbol{\mathcal{F}}^{-1}_{\mathrm{FFT}}\tilde{\mathbf{g}} &(110)\\ \tilde{\mathbf{h}}_1 &= \boldsymbol{\mathcal{F}}_{\mathrm{FFTr}}(\Re\tilde{\mathbf{r}}) &(111)\\ \tilde{\mathbf{h}}_2 &= \boldsymbol{\mathcal{F}}_{\mathrm{FFTr}}(\Im\tilde{\mathbf{r}}) &(112)\\ \mathbf{r}_{\mathrm{e}} &= a_0\Re\tilde{\mathbf{r}} + \sum_{l=1}^{\lfloor (L-1)/2\rfloor} a_{2l}\tilde{\boldsymbol{\omega}}^{2l}\boldsymbol{\mathcal{F}}^{-1}_{\mathrm{FFTh}}(\tilde{\boldsymbol{\tau}}^{2l}\tilde{\mathbf{h}}_1) &(113)\\ \mathbf{r}_{\mathrm{o}} &= \sum_{l=1}^{\lceil (L-1)/2\rceil} b_{2l-1}\tilde{\boldsymbol{\omega}}^{2l-1}\boldsymbol{\mathcal{F}}^{-1}_{\mathrm{FFTh}}(\tilde{\boldsymbol{\tau}}^{2l-1}\tilde{\mathbf{h}}_2) &(114)\\ \mathbf{r} &= \mathbf{r}_{\mathrm{e}} - \mathbf{r}_{\mathrm{o}}. &(115)\end{aligned}$$

Here, $\mathbf{w}_{\mathrm{lo}}$ and $e^{i\boldsymbol{\omega}\tau_c}$ are discrete versions of w_{lo} and $e^{i\tilde{\omega}\tau_c}$, respectively, $\boldsymbol{\mathcal{F}}_{\mathrm{FFTr}}$ is an FFT-based discrete version of $\mathcal{F}$ for real input data and Hermitian output data [28], and $\boldsymbol{\mathcal{F}}^{-1}_{\mathrm{FFTh}}$ is an FFT-based discrete version of $\mathcal{F}^{-1}$ for Hermitian input data and real output data. In (110), $\overline{\tilde{\mathbf{f}}_{\mathrm{lo}}}$ denotes the complex conjugate of $\tilde{\mathbf{f}}_{\mathrm{lo}}$, $|\cdot|$ denotes pointwise magnitude, $\overline{\tilde{\mathbf{f}}_{\mathrm{lo}}}|\tilde{\mathbf{f}}_{\mathrm{lo}}|^{-1}$ is an approximation to $e^{-i(\phi-\omega_c\tau_c)}$, and $\tilde{\mathbf{r}}$ is an approximation to $\mathcal{F}^{-1}\tilde{h}$. We refer to this variant of algorithm CPR-P as CPR-P-r, as it relies on the rotational symmetry of the time map.

The advantage of algorithm CPR-P-r over the original version is that $\boldsymbol{\mathcal{F}}^{-1}_{\mathrm{FFTh}}$ can be made nearly two times faster than $\boldsymbol{\mathcal{F}}^{-1}_{\mathrm{FFT}}$. Part of this gain, however, is lost by the computational effort for (109)–(112). Due to the additional approximations involved, algorithm CPR-P-r may not be quite as accurate as algorithm CPR-P. It has been found experimentally that the range of acquisition times for which algorithm CPR-P-r provides good results can be extended by subtracting $e^{i\tilde{\boldsymbol{\omega}}\tau_c}|\tilde{\mathbf{f}}_{\mathrm{lo}}|$ from the $\tilde{\mathbf{r}}$ in (110) and adding $|\tilde{\mathbf{f}}_{\mathrm{lo}}|$ to the $\mathbf{r}$ in (115).

To some extent, it is possible to deblur spiral MRI images without explicit knowledge of a frequency map. The starting point for such methods is algorithm CPR-DFE-NN. The functions c_l required for this algorithm are not known initially, but can be guessed by an iterative procedure based on the assumption that r_{hi} in (86) should be real. Deblurring algorithms of this kind are described in [7] and [35].

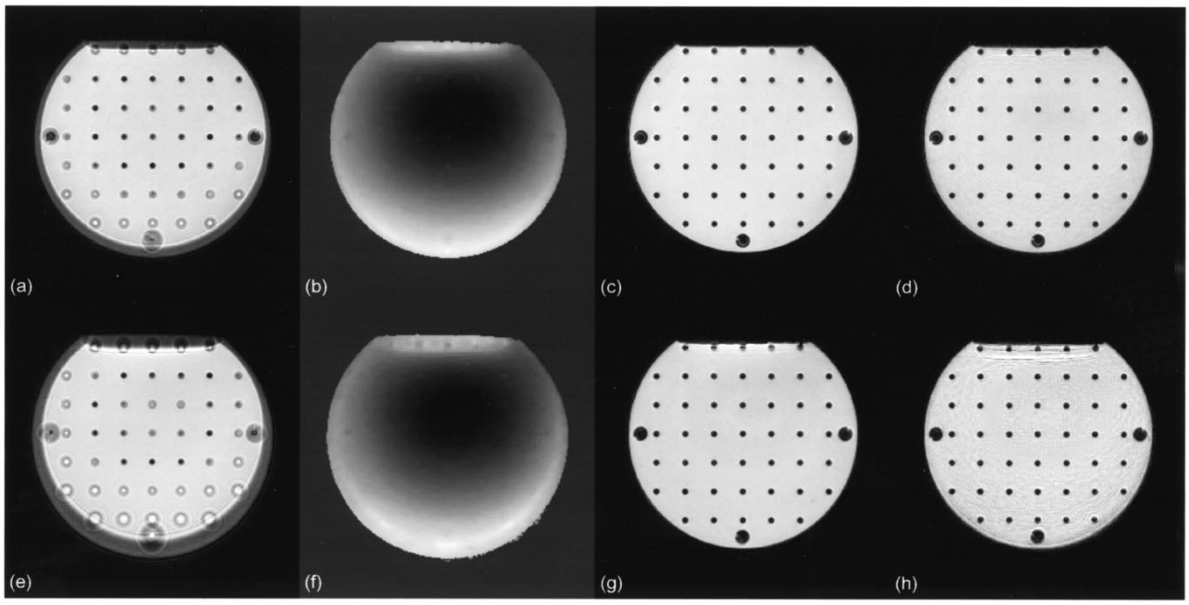

Fig. 2. (a) and (e) Standard spiral MR images of a phantom. (b) and (f) Estimated field maps. (c) and (g) Best possible CPR images. (d) and (h) Best possible SPHERE images. The associated acquisition times are 20 ms (top row) and 40 ms (bottom row).

Algorithm CPR-P-r and the mentioned deblurring algorithms are also applicable to radial MRI. The natural time map of radial MRI is given by (84) with $\psi^{-1}(u) = u$.

VII. Test Results

The various reconstruction algorithms presented in Sections IV–VI were tested on standard images of a phantom. The phantom consisted of a cylindrical plastic container filled with NaCl- and $CuSO_4$-doped water. A 2-D array of thin plastic rods served to make "holes" in the water. A cross-sectional slice of this phantom was imaged in a series of MRI experiments. The MRI system was a 1.5 T Philips Gyroscan NT equipped with shielded gradient coils. The phantom was positioned in the center of the bore with its longitudinal axis parallel to the axis of the magnet. The MR data were acquired with an ordinary spiral pulse sequence, using a standard excitation pulse and no π pulse during the preparation phase. In all cases, the flip angle of the excitation pulse was 45°, the slice thickness 8 mm, and the repetition time 100 ms. The acquisition time, T, was either 10, 20, 40, or 60 ms. The number of spirals, M, was set to 36, 18, 9, or 6, respectively. The spirals were chosen as described in Section VI with $d = 1$ mm, $K = 256$, and $\psi = \psi_{0.25}$. In all cases, the maximum gradient strength and the maximal slew rate were 16.40 mT/m and 31.48 mT/m/ms, respectively. The number of samples per acquisition, N, was set to K^2/M in all cases. For each acquisition time, two MRI experiments with preparation times $T_\mathrm{p} = 2$ ms and $T_\mathrm{p} = 3$ ms were made.

Using a phantom has the advantage that its true image is known. The above experimental setup also ensures that the error term in (5) is relatively small. As the true frequency map is the same in all cases, the size of the off-resonance effect is solely determined by the size of T.

All postprocessing of the MR data was done on a Sun Microsystems Sparcstation 20. The computer programs were written in C, using single precision floating point arithmetic throughout. Computation times were measured by calling the standard C-library function clock() at the beginning and the end of the program. The resulting computation times include the overhead caused by the operating system. A 2-D 256^2 complex FFT takes about 0.5 s on this platform.

In all cases, the image size was $K = 256$ and the pixel size $d = 1$ mm. Standard images of the phantom were reconstructed using an adaptation of the general gridding method described in [33] to spiral MRI. The implementation achieves a reconstruction time of about 3.7 s per image. Fig. 2(a) and (e) shows the standard images at $T = 20$ ms and at $T = 40$ ms, respectively. As expected, the amount of blur grows with T. At $T = 40$ ms there is also some distortion near the top of the phantom. The standard images at $T = 10$ ms and $T = 60$ ms continue the trend in the respective directions and are not shown here. To obtain a sharp standard image of this phantom with this MRI system, an acquisition time of 5 ms or less is required.

Frequency maps were extracted from the two standard images acquired at each acquisition time. The procedure involves a phase unwrapping step, a masking step to set the frequency map to zero outside the estimated support of the image, and a 2-D median filter. The computation of a frequency map takes about 2.4 s, excluding the reconstruction time for the two standard images. Fig. 2(b) shows the estimated frequency map at $T = 20$ ms. The minimum and maximum frequencies within the estimated support of the image are $\omega_-/(2\pi) = -27$ Hz and $\omega_+/(2\pi) = 131$ Hz, resulting in a frequency span of $\Omega/(2\pi) = 158$ Hz. The estimated frequency map at $T = 40$ ms is shown in Fig. 2(f) and has a frequency span of $\Omega/(2\pi) = 166$ Hz. The two frequency maps are almost identical inside the phantom but differ near its boundary. Again, the frequency maps estimated at $T = 10$ ms and $T = 60$ ms continue the trend in the respective directions and are not shown here.

For each acquisition time, the standard image obtained with

a preparation time of 2 ms was postprocessed with each of the CPR algorithms presented in Sections IV and VI, using the frequency map associated with the same acquisition time. Here is a summary of the findings.

As expected, the images produced by the various CPR algorithms become better as L increases. At each acquisition time, there is even a best possible CPR image that most of these algorithms are able to produce if only L is large enough. At $T = 10$ ms and $T = 20$ ms, the best possible CPR images are practically free of blur and distortion. At $T = 40$ ms and $T = 60$ ms, some blur and distortion remains near the top and the bottom of the phantom. Fig. 2(c) and (g) shows the best possible CPR images at $T = 20$ ms and at $T = 40$ ms, respectively. As usual, the best possible CPR images at $T = 10$ ms and $T = 60$ ms continue the trend in the respective directions. However, at $T = 60$ ms the remaining artifacts near the top of the phantom are so large that one is inclined to call them unacceptable.

On the other hand, there are substantial differences between the various CPR algorithms with respect to their behavior as L grows from small to large. For example, algorithm CPR-DFE-NN, when L is small, produces images that are still a bit blurred. As L increases, the images converge slowly but steadily toward the best possible CPR image. Algorithm CPR-P exhibits a totally different behavior. When L is below some threshold value L_θ (which depends on T and presumably on Ω), the images produced by this algorithm show low-frequency wavy artifacts. As L grows beyond the threshold L_θ, these artifacts disappear completely and the resulting images converge very rapidly to the best possible CPR image. Algorithm CPR-DFE-T exhibits a similar but less pronounced threshold behavior. The proper choice of the parameters β_1 and β_2 in (57)–(61) is critical for the performance of this algorithm. As β_1 and β_2 are related via (57), it suffices to choose only one of them. A good recipe, found experimentally, is to set $\beta_2 = L/N$ where N is either $\lfloor\sqrt{\Omega T/(2\pi)}\rfloor$ or $\lfloor\sqrt{L\Omega T/(2\pi)}\rfloor - 1$ and chosen such that $L-N$ is odd. (Among other things, this choice ensures that τ_- and τ_+ are among the τ_k.) Algorithm CPR-DTE-NN requires extremely many terms to produce images that come close to the best possible CPR image. Algorithm CPR-DTE-T behaves roughly like algorithm CPR-DFE-T. However, a simple rule for deriving good choices of the parameters β_1 or β_2 from L or ΩT could not be found. Finally, algorithm CPR-P-r produces good magnitude images at $T = 10$ ms and $T = 20$ ms, but not at $T = 40$ ms and $T = 60$ ms. Fig. 3(a) and (b) shows the best possible images produced by this algorithm at $T = 20$ ms and at $T = 40$ ms, respectively. The choice of the parameter α_1 in (88) is not critical: a good choice is $\alpha_1 = 0.25$.

The four SPHERE algorithms SPH-DFE-T, SPH-DTE-NN, SPH-DTE-T, and SPH-P were also tested. Again, there is a best possible SPHERE image for each acquisition time. However, except at $T = 10$ ms, the image quality of the best possible SPHERE images is noticeably inferior to that of the best CPR images obtained at the same T. Fig. 2(d) and (h) shows the best possible SPHERE images at $T = 20$ ms and at $T = 40$ ms, respectively. Otherwise, the SPHERE algorithms behave roughly like their CPR counterparts.

In practice, one wants to compute a reasonably good CPR or SPHERE image as fast as possible. Thus, for each algorithm and acquisition time, an attempt was made to find out the number of terms required for a reasonably good CPR or SPHERE image, respectively. Table I lists the results for each acquisition time and for each algorithm that could produce a reasonably good image at this acquisition time. The columns labeled L list the number of terms required for the reasonably good image. The associated computation times are listed in the adjacent columns. The goodness of an image $\mathbf{f}$ was measured by the relative error $\| |\mathbf{f}| - |\mathbf{f}_{\rm opt}| \| / \|\mathbf{f}_{\rm opt}\|$ where $|\cdot|$ denotes pointwise magnitude, $\|\cdot\|$ denotes the Euclidean norm in $\mathbb{C}^{KK}$, and $\mathbf{f}_{\rm opt}$ is the pertinent best possible CPR or SPHERE image. Table I also lists the relative error in each case. The best possible CPR and SPHERE images were computed by algorithms CPR-DFE-T and SPH-DFE-T, respectively, using a very large number of terms. As the above measure of goodness is sometimes misleading, it was combined with a subjective judgment based on visual inspection. The step behavior of the P-class algorithms makes it easy to identify the number of terms required for a reasonably good CPR image. For the T-class algorithms, which have a less marked step behavior, this number of terms is less well defined and remains a little ambiguous. For the table, the smallest possible number was selected. For the best image quality, one or two more terms are needed. For the two DFE-T algorithms the parameter β_2 was chosen as described above. For the two DTE-T algorithms good values for β_1 were determined by trial and error. For the NN-class algorithms, which exhibit no step behavior at all, the number of terms was chosen via (52) with $\beta = 2.5$ for algorithm CPR-DFE-NN and $\beta = 10$ for the two DTE-NN algorithms. These choices provide a good compromise between image quality and computation time.

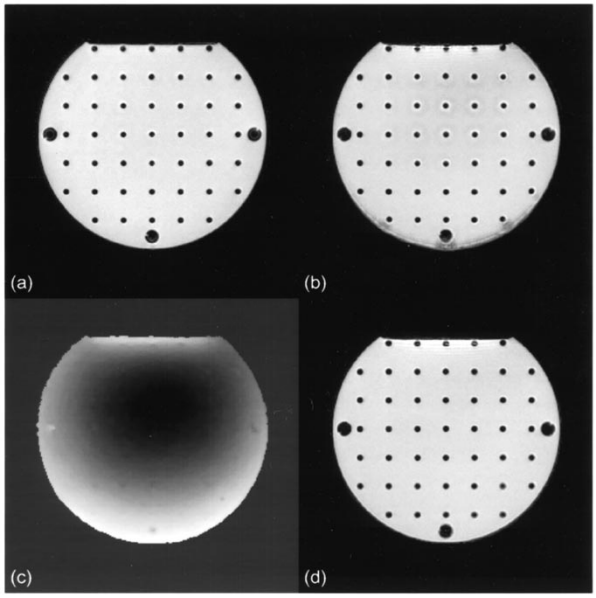

Fig. 3. (a) Best possible image produced by algorithm CPR-P-r at $T = 20$ ms. (b) Best possible image produced by algorithm CPR-P-r at $T = 40$ ms. (c) Iterated frequency map at $T = 40$ ms. (d) Best possible CPR image at $T = 40$ ms, recomputed with the iterated frequency map shown in (c).

At $T = 40$ ms and $T = 60$ ms, the table contains the results for the three algorithms CPR-DFE-NN, CPR-DFE-T, and

TABLE I
TEST RESULTS

algorithm	L	run time	rel. error	$\frac{2\pi L}{\Omega T}$	comments	L	run time	rel. error	$\frac{2\pi L}{\Omega T}$	comments
	$T = 10$ ms, $\Omega/(2\pi) = 158$ Hz, $\Omega T/(2\pi) = 1.58$					$T = 20$ ms, $\Omega/(2\pi) = 166$ Hz, $\Omega T/(2\pi) = 3.32$				
CPR-DFE-NN	4	3.4 s	0.019	2.53		9	6.2 s	0.017	2.71	
CPR-DFE-T	5	4.1 s	0.015	3.16	$\beta_2 = 2.50$	9	6.4 s	0.010	2.71	$\beta_2 = 2.25$
CPR-DTE-NN	16	9.7 s	0.021	10.13		34	19.3 s	0.026	10.24	
CPR-DTE-T	9	6.6 s	0.011	5.70	$\beta_1 = 2.66$	11	7.9 s	0.014	3.31	$\beta_1 = 1.49$
CPR-P	6	4.2 s	0.002	3.80		9	5.8 s	0.009	2.71	
CPR-P-r	3	3.1 s	0.027	1.90	$\alpha_1 = 0.25$	6	3.9 s	0.038	1.81	$\alpha_1 = 0.25$
SPH-DFE-T	7	7.1 s	0.015	4.43	$\beta_2 = 3.50$	12	11.1 s	0.016	3.61	$\beta_2 = 2.40$
SPH-DTE-NN	16	9.2 s	0.019	10.13		34	18.3 s	0.021	10.24	
SPH-DTE-T	8	6.0 s	0.016	5.06	$\beta_1 = 2.31$	14	9.7 s	0.010	4.22	$\beta_1 = 2.10$
SPH-P	6	4.7 s	0.004	3.80		9	6.4 s	0.010	2.71	
	$T = 40$ ms, $\Omega/(2\pi) = 174$ Hz, $\Omega T/(2\pi) = 6.98$					$T = 60$ ms, $\Omega/(2\pi) = 179$ Hz, $\Omega T/(2\pi) = 10.72$				
algorithm	L	run time	rel. error	$\frac{2\pi L}{\Omega T}$	comments	L	run time	rel. error	$\frac{2\pi L}{\Omega T}$	comments
CPR-DFE-NN	18	10.9 s	0.020	2.58		27	15.8 s	0.022	2.52	
CPR-DFE-T	14	9.3 s	0.009	2.01	$\beta_2 = 1.56$	19	12.2 s	0.012	1.77	$\beta_2 = 1.36$
CPR-P	16	9.5 s	0.005	2.29		22	12.6 s	0.018	2.05	round. errs.

CPR-P only. At these acquisition times, algorithm CPR-P-r and all SPHERE algorithms were unable to produce acceptable images at all, algorithm CPR-DTE-NN was definitely too slow, and algorithm CPR-DTE-T was discarded because it lacks a known practicable way to determine good values for its parameters.

With respect to image quality per number of terms, algorithms CPR-DFE-NN, CPR-DFE-T, and CPR-P are clearly the best among the tested CPR algorithms. Algorithm CPR-P-r is the fastest, but restricted to images with small and medium size off-resonance artifacts. At $T = 60$ ms, algorithm CPR-P begins to suffer from rounding errors, but in this regime the CPR approach, as such, is already of limited value. Among the SPHERE algorithms, algorithm SPH-P is the clear winner.

The table also lists the quantity $2\pi L/(\Omega T)$, which is the maximum value of the parameter β that would produce L via (52). The results suggest that L might be chosen as in (52), where β depends on the algorithm and is otherwise constant or a slowly varying function of ΩT that may be predetermined and tabulated.

An attempt was made to improve the best possible CPR image at $T = 40$ ms by using an iterated frequency map, as indicated at the end of Section II. Fig. 3(c) and (d) shows the iterated frequency map and the recomputed best possible CPR image, respectively. The distortion near the top of the phantom has disappeared, but some ripples remain.

CPR with post-iteration was also tried, but did not yield satisfactory results. In hindsight, this may be understood. The iteration attempts to change the image at places where CPR by itself is not very accurate, but these are also the places where the frequency map is likely to be inaccurate.

The better of the CPR algorithms were also applied to a standard spiral MR image of a transverse cross section of a human brain. To obtain this image, the excitation phase of the pulse sequence was augmented by a standard fat suppression technique [36]. The flip angle of the excitation pulse was now 60°, the slice thickness 7 mm, the acquisition time $T = 20$ ms, and the repetition time 1000 ms. The number of spirals was set to $M = 15$, resulting in a maximum gradient strength of about 20 mT/m. Again, the image size was $K = 256$ and the pixel size $d = 1$ mm. The standard image is shown in Fig. 4(a). The associated estimated frequency map is shown in Fig. 4(b). Its frequency span is $\Omega/(2\pi) = 388$ Hz so that $\Omega T/(2\pi) = 7.67$. The variation of the frequency map in and

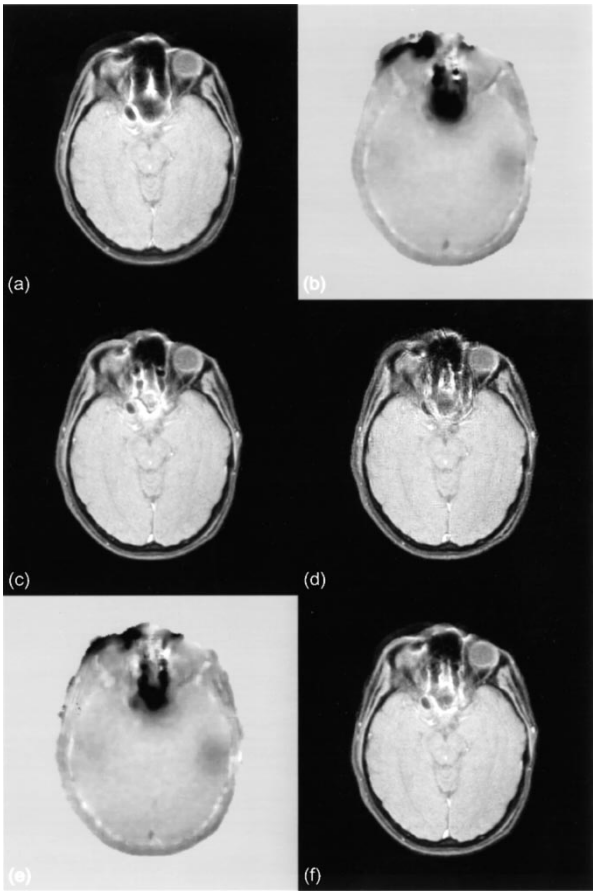

Fig. 4. (a) Standard spiral MR image of a human brain obtained at $T = 20$ ms. (b) Associated frequency map. (c) Best possible CPR image. (d) Best possible SPHERE image. (e) Iterated frequency map. (f) Best possible CPR image recomputed with the iterated frequency map shown in (e).

near the nasal cavities is extreme. The best possible CPR and SPHERE images associated with this frequency map are shown in Fig. 4(c) and (d), respectively. The improvement of the CPR image near the eyes and at the back of the head is noticeable. Again, the appearance of the SPHERE image is less satisfactory than that of the CPR image. Both images have also changed significantly in and near the nasal cavities, but given the strong variation of the frequency map there, the accuracy of the images in this region may be questioned. Fig. 4(e) and (f) shows the iterated frequency map and the recomputed best possible CPR image, respectively. The image has changed in and near the nasal cavities, but its accuracy there remains doubtful.

VIII. Concluding Remarks

The results reported in this paper suggest that the approximate inversion of the MR transform via CPR is a viable method to remove off-resonance artifacts from standard spiral MR images. The approach allows one to reduce the number of spirals by a factor between four to eight and still obtain sharp spiral MR images.

The three CPR algorithms CPR-DFE-NN, CPR-DFE-T, and CPR-P can be recommended. Algorithm CPR-P-r is appropriate when speed counts most.

The results also suggest that the approximate inversion of the MR transform by SPHERE is less accurate than an approximate inversion by CPR, at least in the case of spiral MRI. For Cartesian MRI the situation may be different, as SPHERE may be able to make a better use of distorted frequency maps [9].

The recommendable CPR algorithms are so fast that they may be executed in real time on a suitable embedded parallel computer comprised of a small number of state-of-the-art microprocessors or digital signal processors.

The required frequency map can be estimated from two standard images in the usual way. In favorable cases, it is conceivable to extract the frequency map from a single standard image. Improved frequency maps may be obtained iteratively, although the computational cost is high. Theoretically, the approximation underlying the CPR approach could be overcome in various ways, but in practice the difficulty of obtaining an accurate frequency map limits the value of such attempts.

Acknowledgment

The author thanks B. Aldefeld for stimulating discussioins, P. Börnert for providing the MR data, and M. Fuderer and the anonymous reviewers for their comments and suggestions.

References

[1] W. S. Hinshaw and A. H. Lent, "An introduction to NMR imaging: From the Bloch equation to the imaging equation," *Proc. IEEE,* vol. 71, pp. 338–350, Mar. 1983.

[2] S. Ljunggren, "A simple graphical representation of Fourier-based imaging methods," *J. Magnetic Resonance,* vol. 54, pp. 338–343, 1983.

[3] D. B. Twieg, "The k-trajectory formulation of the NMR imaging process with applications in analysis and synthesis of imaging methods," *Med. Phys.,* vol. 10, no. 5, pp. 610–621, 1983.

[4] K. F. King and P. R. Moran, "A unified description of NMR imaging, data-collection strategies, and reconstruction," *Med. Phys.,* vol. 11, no. 1, pp. 1–14, 1984.

[5] R. T. Vlaardingerbroek and J. A. den Boer, *Magnetic Resonance Imaging.* Berlin, Germany: Springer-Verlag, 1996.

[6] D. C. Noll, C. H. Meyer, J. M. Pauly, D. G. Nishimura, and A. Macovski, "A homogeneity correction method for magnetic resonance imaging with time-varying gradients," *IEEE Trans. Med. Imag.,* vol. 10, pp. 629–637, Dec. 1991.

[7] D. C. Noll, J. M. Pauly, C. G. Meyer, D. G. Nishimura, and A. Macovski, "Deblurring for non-2D Fourier transform magnetic resonance imaging," *Magnetic Resonance Med.,* vol. 25, pp. 319–333, 1992.

[8] L.-C. Man, J. M. Pauly, and A. Macovski, "Multifrequency interpolation for fast off-resonance correction," *Magnetic Resonance Med.,* vol. 37, pp. 785–792, 1997.

[9] Y. M. Kadah and X. Hu, "Simulated phase evolution rewinding (SPHERE): A technique for reducing B_0 inhomogeneity," *Magnetic Resonance Med.,* vol. 38, pp. 615–627, 1997.

[10] R. Bhagwandien, R. van Ee, R. Beersma, C. J. G. Bakker, M. A. Moerland, and J. J. W. Lagendijk, "Numerical analysis of the magnetic field for arbitrary magnetic susceptibility distributions in 2D," *Magnetic Resonance Imag.,* vol. 10, pp. 299–313, 1992.

[11] ——, "Numerical analysis of the magnetic field for arbitrary magnetic susceptibility distributions in 3D," *Magnetic Resonance Imag.,* vol. 12, pp. 101–107, 1994.

[12] T. S. Sumanaweera, G. H. Glover, T. O. Binford, and J. R. Adler, "MR susceptibility misregistration correction," *IEEE Trans. Med. Imag.,* vol. 12, pp. 251–259, June 1993.

[13] C. E. Hayes and P. B. Roemer, "Noise correlations in data simultaneously acquired from multiple surface coil arrays," *Magnetic Resonance Med.,* vol. 16, pp. 181–191, 1990.

[14] W. A. Edelstein, J. M. S. Hutchison, G. Johnson, and T. Redpath, "Spin-warp NMR imaging and applications to human whole-body imaging," *Phys. Med. Biol.,* vol. 25, pp. 751–756, 1980.

[15] M. J. Stehling *et al.,* "Whole-body echo-planar MR imaging at 0.5 T," *Radiology,* vol. 170, no. 1, pp. 257–263, 1989.

[16] K. Butts, S. J. Riederer, R. L. Ehman, R. M. Thompson, and C. R. Jack, "Interleaved echo planar imaging on a standard MRI system," *Magnetic Resonance Med.,* vol. 31, pp. 67–72, 1994.

[17] S.-G. Kim, X. Hu, G. Adriany, and K. Ugurbil, "Fast interleaved echo-planar imaging with navigator: High resolution anatomic and functional images at 4 Tesla," *Magnetic Resonance Med.,* vol. 35, pp. 895–902, 1996.

[18] R. S. Likes, "Moving gradient zeugmatography," U. S. Patent 4 307 343, 1981.

[19] B. C. Ahn, J. H. Kim, and Z. H. Cho, "High-speed spiral-scan echo planar NMR imaging—I," *IEEE Trans. Med. Imag.,* vol. MI-5, pp. 2–7, Jan. 1986.

[20] C. H. Meyer, B. S. Hu, D. G. Nishimura, and A. Macovski, "Fast spiral coronary artery imaging," *Magnetic Resonance Med.,* vol. 28, pp. 202–213, 1992.

[21] P. C. Lauterbur, "Image formation by induced local interaction: Examples employing nuclear magnetic resonance," *Nature,* vol. 242, pp. 190–191, 1973.

[22] P. Mansfield and P. G. Morris, *NMR Imaging in Biomedicine.* New York: Academic, 1982.

[23] A. B. Kerr, J. M. Pauly, B. S. Hu, K. C. Li, C. J. Hardy, C. H. Meyer, A. Macovski, and D. G. Nishimura, "Real-time interactive MRI on a conventional scanner," *Magnetic Resonance Med.,* vol. 38, pp. 355–367, 1997.

[24] M. Reed and B. Simon, *Methods of Modern Mathematical Physics I: Functional Analysis.* New York: Academic, 1980.

[25] K. Sekihara, S. Matsui, and H. Kohno, "NMR imaging for magnets with large nonuniformities," *IEEE Trans. Med. Imag.,* vol. MI-4, pp. 193–199, Dec. 1985.

[26] A. Maeda, K. Sano, and T. Yokoyama, "Reconstruction by weighted correlation for MRI with time-varying gradients," *IEEE Trans. Med. Imag.,* vol. 7, pp. 26–31, Jan. 1988.

[27] S. J. Norton, "Fast magnetic resonance imaging with simultaneously oscillating and rotating gradients," *IEEE Trans. Med. Imag.,* vol. MI-6, pp. 21–31, Jan. 1987.

[28] W. H. Press, S. A. Teukolsky, W. T. Vetterling, and B. P. Flannery, *Numerical Recipies in C,* 2nd ed. Cambridge, U.K.: Cambridge Univ. Press, 1992.

[29] F. John, "Integral equations," in *Mathematics Applied to Physics,* É. Roubine, Ed. Berlin, Germany: Springer-Verlag, 1970, pp. 316–347.

[30] Y. M. Kadah and X. Hu, "Algebraic reconstruction for magnetic resonance imaging under B_0 inhomogeneity," *IEEE Trans. Med. Imag.,*

vol. 17, pp. 362–370, June 1998.
[31] W. N. Brouw, "Aperture synthesis," in *Methods in Computational Physics*, B. Alder, S. Fernbach, and M. Rotenberg, Eds. New York: Academic, 1975, vol. 14, pp. 131–175.
[32] J. I. Jackson, C. H. Meyer, D. G. Nishimura, and A. Macovski, "Selection of a convolution function for Fourier inversion using gridding," *IEEE Trans. Med. Imag.*, vol. 10, pp. 473–478, Sept. 1991.
[33] H. Schomberg and J. Timmer, "The gridding method for image reconstruction by Fourier transformation," *IEEE Trans. Med. Imag.*, vol. 14, pp. 596–607, Sept. 1995.
[34] G. Dahlquist and Å. Björck, *Numerical Methods.* Englewood Cliffs, NJ: Prentice-Hall, 1974.
[35] L.-C. Man, J. M. Pauly, and A. Macovski, "Improved automatic off-resonance correction without a field map in spiral imaging," *Magnetic Resonance Med.*, vol. 37, pp. 906–913, 1997.
[36] A. Haase, W. Frahm, J. Hänicke, and D. Matthaei, "^{1}H NMR chemical shift selective (CHESS) imaging," *Phys. Med. Biol.*, vol. 30, pp. 341–3344, 1985.